A new spectral harmonization algorithm for Landsat-8 and Sentinel-2 remote sensing reflectance products using machine learning: a case study for the Barents Sea (European Arctic)

Muhammad Asim, Atsushi Matsuoka, Pål Gunnar Ellingsen, Camilla Brekke, Member IEEE, Torbjørn Eltoft, Member IEEE, and Katalin Blix

***Abstract*—The synergistic use of Landsat-8 Operational Land Imager (OLI) and Sentinel-2 Multispectral Instrument (MSI) data products provides an excellent opportunity to monitor the dynamics of aquatic ecosystems. However, the merging of data products from multi-sensors is often adversely affected by the difference in their spectral characteristics. In addition, the errors in the atmospheric correction (AC) methods further increase the inconsistencies in downstream products. This work proposes an improved spectral harmonization method for OLI and MSI-derived remote sensing reflectance (R_{rs}) products, which significantly reduces uncertainties compared to those in the literature. We compared the R_{rs} retrieved via state-of-the-art AC processors, i.e., Acolite, C2RCC, and Polymer, against ship-based in-situ R_{rs} observations obtained from the Barents Sea waters, including a wide range of optical properties. Results suggest that the Acolite-derived R_{rs} has a minimum bias for our study area with median absolute percent difference (MAPD) varying from 9 to 25% in the blue-green bands. To spectrally merge OLI and MSI, we develop and apply a new machine learning-based bandpass adjustment (BA) model to near-simultaneous OLI and MSI images acquired in the years from 2018 to 2020. Compared to a conventional linear adjustment, we demonstrate that the spectral difference is significantly reduced from ~6 to 12% to ~2 to $<10\%$ in the common OLI-MSI bands using the proposed BA model. The findings of this study are useful for the combined use of OLI and MSI R_{rs} products for water quality monitoring applications. The proposed method has the potential to be applied to other waters.**

***Index Terms*—Barents Sea, Ocean Color, intersensor-comparison, remote sensing reflectance, machine learning.**

I. INTRODUCTION

THE Barents Sea is the northernmost Arctic shelf sea and one of the most productive oceans in the world [1]. It contributes up to 40% of the total primary production in the Arctic system [2] and represents an ultimate region for exploring and monitoring the impact of Arctic climate change [1]. The Barents Sea is experiencing significant alterations in its physical and biological characteristics in response to the ongoing global warming [3], [4]. The surface is exposed to prolonged exposure to sunlight during summer and fall, leading to a decrease in sea ice extent and an increase in the production and seasonal growth of phytoplankton [4].

Understanding the effect of altered physical and environmental conditions on the ecosystem of the transitional Barents Sea requires temporally frequent monitoring of the biogeochemical changes occurring in the water columns [5]. Traditional ship-based sampling takes place discontinuously, is time-consuming, and is expensive. Alternatively, satellite derived remote sensing reflectance (R_{rs}) can be used to derive in-water constituents, such as Chlorophyll-a (Chl-a), offers broad spatial coverage, repeated overpasses, and is of relatively low cost [6], [7]. Accurate and consistent retrieval of R_{rs} is therefore a vital step towards the estimation of biogeochemical quantities from remotely sensed data [8].

Capturing an abrupt biological phenomenon such as phytoplankton spring blooms from space requires the acquisition of ocean color imagery with short time intervals (2–3 days) at a high spatial resolution ($<$ 60 m) [9], [10]. However, most of the existing ocean color sensors with a higher temporal resolution, including the Ocean and Land Color Imager (OLCI) onboard Sentinel-3A/B, Moderate Resolution Imaging Spectroradiometer (MODIS), Geostationary Ocean Color Imager (GOCI), Visible Infrared Imaging Radiometer Suite (VIIRS), Second-generation Global Imager (SGLI), as well as the upcoming PACE Ocean Color Instrument (PACE-OCI), have a much coarser spatial resolution (250-1000 m). This reduces their suitability for detecting fine features in natural waters [11], [12].

In contrast, high spatial resolution satellite sensors such as the Operational Land Imager (OLI) on-board Landsat-8 (L8) and the Multispectral Imager (MSI) on-board Sentinel-2A/2B (S2-A/B) with spatial resolution <60 m, have considerable potential for observing the optical quality of water bodies with more spatially-detailed information not feasible with other ocean color sensors. However, these two sensors have individually a low-frequency revisit time of 16 days for OLI and 5 days for MSI, respectively, [13], not sufficient for near-daily monitoring of the water surface [11].

M. Asim, K. Blix, C. Brekke and T. Eltoft are with the Department of Physics and Technology, UiT The Arctic University of Norway (UiT), Tromsø, Norway, e-mails: {muhammad.asim, camilla.brekke, torbjørn.eltoft}@uit.no.

A. Matsuoka is with the Institute for the Study of Earth, Oceans, and Space, University of New Hampshire, Durham, NH, 03824, USA, e-mail: {atsushi.matsuoka}@unh.edu.

P. Ellingsen is with the Department of Electrical Engineering, UiT The Arctic University of Norway, Narvik, Norway, e-mail: {pal.g.ellingsen}@uit.no.

The optical remote sensing of the Barents Sea is associated with several challenges. Being an aquatic system in the high north, it experiences polar night during the winter season and is frequently covered by clouds in the summer, which severely limits the availability of cloud-free scenes to work with. Furthermore, for accurate retrieval of water quality (WQ) parameters, the elimination of the atmospheric influence is essential. Atmospheric correction (AC) is particularly challenging in the high north due to long ray paths caused by the higher solar zenith angles and adjacency of sea ice, and there is uncertainty associated with the validity of existing AC methods [14].

To optimize the availability of ocean color data for regular monitoring of the Barents Sea waters during summer months, it would be most favourable to combine MSI and OLI observations [13]. L8 OLI and S2 MSI have the same band design and provide similar observations; however, they are not strictly identical. These sensors have different fields of view (FOV), spatial resolution, spectral bandwidth, and spectral response functions (SRFs) [9], [15]. Such differences lead to inconsistencies in downstream data products such as the R_{rs} and the biogeochemical quantities derived from diagnostic R_{rs} signature [16]. The differences introduced by spatial resolution and FOV can be reduced by minimizing the bidirectional reflectance distribution factors (BRDFs) [17]; however, the spectral differences caused by SRF's and spectral bandwidths remain a challenging task for developing seamless products. The difference in the SRFs' of the sensors increases the differences in the pixel values, which in turn create variations in spectral index values and can lead to misinterpretations of the results [16].

In this paper, we study the merging of MSI and OLI imagery for water surface monitoring in the high north by addressing two key aspects: i) We investigate whether the use of standard AC algorithms results in realistic R_{rs} values at these latitudes. ii) We develop a comprehensive method for merging OLI and MSI data products by introducing a new band adjustment (BA) method.

It is noted that to account for the differences in relative SRF's of S2 MSI and L8 OLI, most of the previous studies have either used linear regression or fixed per-band regression coefficients to reduce the spectral difference between L8 and S2-derived R_{rs} products [9], [11], [15], [18], [19]. Pahlevan et al. used a machine learning (ML) based technique, originally developed in [20], to predict MSI-derived R_{rs} from those derived from OLI [10]. They simulated hyperspectral ρ_t using MODTRAN code for each matchup site and processed through SeaDAS to generate R_{rs} using vicarious gains. Similarly authors in [21] used simulated MSI-OLI synergies to monitor dissolved organic carbon (DOC) fluxes in Arctic rivers [21]. With a goal of producing consistent multi-mission global WQ indicators, the authors in [22] evaluated the performance of retrieval models for estimating WQ indicators from near-simultaneous images of OLI, MSI, and OLCI sensors. Wang et al. evaluated the consistency of suspended particulate matter (SPM) concentrations retrieved from same-day OLI-MSI overpasses in turbid waters and reported that the consistency in SPM concentrations is highly dependent on the performance of the AC [23]. Some studies have used combined OLI-MSI images to enable the monitoring of lake and river waters; however, the cross-sensor performance was validated using only 1-4 coincident same-day overpasses [24]–[26]. Other studies have evaluated the spectral consistency between OLI-MSI R_{rs} products without validating against the in-situ R_{rs} data [18], [19], [27]–[29]. This leads to uncertainties in satellite-derived R_{rs} estimates, which in turn affect the estimation of biogeochemical quantities [8]. As per our knowledge, no study has been reported on the validation of AC using S2 or L8 in the Barents Sea, restricting match-ups in the time window of within ± 3 hours recommended for validating ocean color products [30].

To achieve spectral harmonization of OLI-MSI R_{rs} products over Barents Sea waters, the present study first evaluates the performance of three state-of-the-art AC models, C2RCC [31], Acolite [32] and Polymer [33] against ship-based in-situ R_{rs} observations. The aforementioned step ensures realistic R_{rs} estimates from satellite images for the study region. The top performing AC scheme was then selected to estimate R_{rs} products from near-simultaneous OLI and MSI images over the Barents Sea region from the year 2018 to 2020, limiting the difference in observations to <30 minutes. Instead of fitting the transformation coefficients of a linear regression model, we propose a new ML-based spectral bandpass adjustment (BA) method for spectral alignment of OLI-MSI R_{rs} products. The proposed spectral BA method is based on a feedforward multilayer perceptron (MLP) developed previously for a different application and data in [34]. The neural network (NN)-based model is tuned to spectrally adjust S2-A/B radiometry to replicate the spectral bandpasses of L8 for the common bands on both sensors. To the best of our knowledge, no such study has been conducted to explore the efficiency of NNs in improving the spectral alignment of OLI-MSI R_{rs} products, particularly over high latitude waters.

Our study provides a detailed analysis of the performance of the three aforementioned AC schemes compared against in-situ R_{rs} observations and an evaluation of inter-sensor spectral consistency between OLI and MSI images based on the new BA method. A flow-chart of the work is shown in Fig. 1. The major contributions of the present study are as follows:

- We have collected ship-based above-water R_{rs} measurements continuously over the course of the ship's route. This novel dataset covers a wide array of atmospheric and aquatic conditions in the Barent Sea.
- Considering in-situ R_{rs} data as a ground truth, performance of Acolite, C2RCC, and Polymer AC schemes are examined.
- We have evaluated the spectral consistency between real L8 and S2 images over the Barents Sea region from 2018 to 2020. To ensure similar aquatic and environmental conditions for inter-sensor comparison, we have considered observations acquired from nearly simultaneous overpasses (< 30 minutes).
- To minimize the spectral differences in R_{rs} products,

This article has been accepted for publication in IEEE Transactions on Geoscience and Remote Sensing. This is the author's version which has not been fully edited and content may change prior to final publication. Citation information: DOI 10.1109/TGRS.2022.3228393

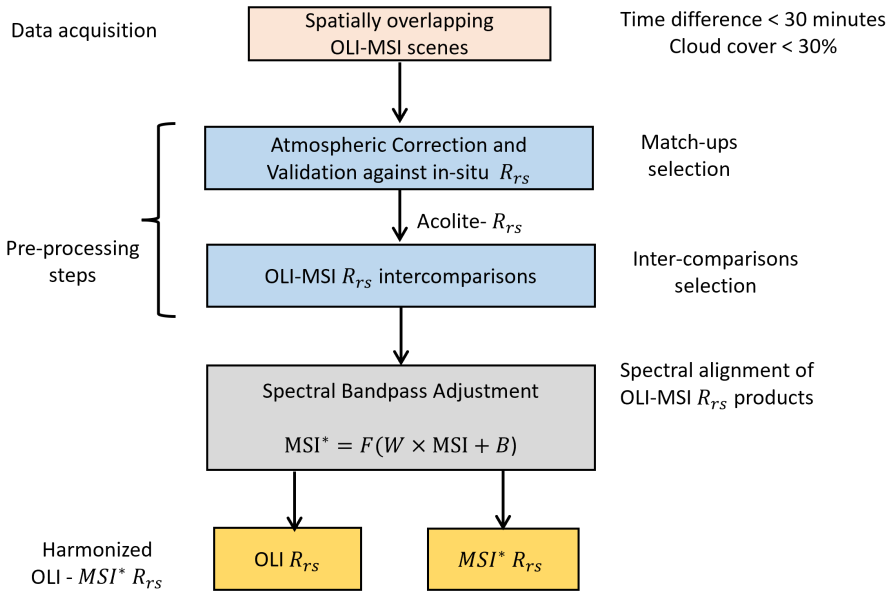

Fig. 1: Flow chart of the proposed spectral harmonization approach with major steps of analysis. i) OLI-MSI scenes acquisition at the top of the atmospheres (TOA) with spatially overlapping region. ii) Validation of Atmospheric correction schemes against the in-situ R_{rs}. The AC scheme in good agreement with in-situ R_{rs} is selected to process near-simultaneous OLI-MSI images. iii) The MSI R_{rs} products are bandpass adjusted to that of OLI R_{rs} products. The proposed BA model minimize the spectral difference in OLI-MSI R_{rs} products. W and B represents weights and biases of the BA model.

we propose a new NN-based algorithm for spectral BA of S2 MSI R_{rs}, using L8 OLI R_{rs} products as a reference.

The present paper is organized as follows: Section II briefly discusses the proposed spectral harmonization method, the AC processors, and the new BA algorithm. Section III presents information on the in-situ and satellite data collection followed by the main methodology, which comprises of two major prepossessing steps, i.e., match-up section (III-B2) and inter-comparison selection (III-B2) before the spectral alignment of OLI-MSI images presented in section III-D. The experimental results are discussed in section IV, which elaborates on the performance of AC schemes against the in-situ R_{rs} followed by inter-comparisons of OLI and MSI R_{rs} products before and after spectral alignment of OLI-MSI R_{rs} products. Finally, conclusions are drawn in section V.

II. Spectral harmonization

To harmonize the remote sensing reflectance (R_{rs}) data from Landsat-8 (L8) and Sentinel-2 (S2) into a single dataset, correction factors must be applied to mitigate the spectral differences in their R_{rs} products [13]. Previous studies have used linear regression models to adjust S2 radiometry to replicate the spectral bandpasses of L8 [9], [11], [15]. The spectral bandpass adjustment (BA) converts atmospherically corrected S2-derived R_rs products to L8-derived products. Therefore, atmospheric correction (AC) is an important step in order to ensure reliable input data before spectral harmonization of their data products. There are several AC algorithms that can be used for spectral harmonization of these sensors. However, the performances of these methods have not yet been evaluated for the Barents Sea waters. This might be due to the lack of in-situ radiometric data. In this work, we first evaluate the performance of AC processors against in-situ observations. The R_{rs} retrieved via top performing AC scheme was then used to harmonize L8 and S2-derived R_{rs} products using the proposed machine learning (ML)-based spectral BA method. In the following subsections (II-A and II-B), we have briefly described the AC processors; the data used for validation of AC methods and the spectral alignment of S2 and L8 R_{rs} products. More details are provided in section III.

A. AC evaluation

1) Data: Sentinel-2A/B (S2-A/B) MultiSpectal Instrument (MSI) images with a time gap of ±3 hours of in-situ observations (see Section III-B1) acquired in the year 2021 were used to compare the AC algorithms' performances (hereafter referred to as match-ups; see Section III-B2 for details).

2) AC processors: The goal of AC is to accurately retrieve R_rs from the received satellite signal rho_t. In this work, we have compared the performance of three AC processors. C2RCC v1.0 [31], Polymer v4.13 [33], and Acolite version 20211124.0 [32].

These AC processors have significant differences in their methods. The Acolite dark spectrum fitting (DSF) scheme relies on black pixel assumption and includes an aerosol model. This scheme is recommended for clear and mixed clear/turbid waters [35]. The C2RCC AC is a machine learning (ML)-based scheme where the neural networks (NNs) are trained on different water types and extreme ranges of scattering and absorption properties [31]. The Polymer scheme, which was primarily developed to work in sun glint regions [33] does not make a black pixel assumption or include an aerosol model, but works on the principle of the per-pixel spectral matching method. These AC processors have shown reasonable success in processing high resolution sensor imagery such as L8 and S2 imagery over global oceanic waters having various optical properties to extremely turbid inland waters [5], [7], [8], [35], [36]. Yet none of them have been evaluated in the Barents Sea region. It should be noted that there is currently no ideal AC processor available for generating seamless $R_r s$ products from these sensors.

B. Spectral BA method

1) Data: To harmonize the R_{rs} products from L8 Operational Land Imager (OLI) and S2 MSI sensors, we have used near-simultaneous overpasses with a time-difference of ≤ ±30 minutes from April to September for 2018-2020 (hereafter referred to as inter-comparisons; see section III-C for details).

2) Method: In the present study, a new machine learning (ML) based algorithm using a fully connected feed-forward Multi-Layer Perceptron (MLP) is developed to minimize the spectral difference between OLI-MSI R_{rs} products. The architecture and systematic system diagram illustrating the main components of the proposed BA method are given in section III-D.

III. Materials and Method

A. Satellite data

In this study, S2-A/B MSI and L8 OLI imagery are used. Details on band characteristics of these satellite sensors are provided in Table. I. Level 1C MSI and Level 1T OLI collection-1 data, calibrated top-of-atmosphere (TOA) reflectance (ρ_t), were acquired from ESA's Copernicus Open Access Hub (https://scihub.copernicus.eu/) and Earth Explorer (https://earthexplorer.usgs.gov/), respectively.

B. Match-ups

1) In-situ data collection and processing: The in-situ above-water measurements were assembled from multiple field campaigns in the year 2021 aboard the Norwegian icebreaker R/V Kronprins Haakon. The data were collected autonomously while the ship was at sea and cover a broad range of aquatic and environmental conditions. A set of TRIOS RAMSES hyper-spectral radiometers (two radiance sensors and one irradiance sensor) were mounted on the ship to collect radiometric data in a spectral range from 320 to 950 nm at ~3 nm resolution, and an integration time of 30 seconds. During each campaign, in addition to the predefined sampling stations where the ship was left free to float during the field measurements, in-situ data were also collected along the transect. This data is the longest record of in-situ radiometric measurements in the Barents Sea in Norwegian territorial waters. In terms of match-up scenes, only S2 cloud-free images with a time gap of ±3 hours with the in-situ observations in the year 2021, are shown in Fig. 2.

The radiometric quantity utilized in this study is the remote sensing reflectance, R_{rs}, defined as $L_w(0^+)/E_d(0^+)$ [37]. Here $L_w(0^+)$ and $E_d(0^+)$ are the water-leaving radiance and downwelling irradiance measured just above the water surface. The R_{rs} is computed using the procedure given in [38]. The processed in-situ R_{rs} spectra were then filtered to eliminate the remaining erroneous measurements using the criteria defined in [7], [38] with some slight modifications as follows:

- Mean R_{rs} intensity in range (350-400 nm) ≥ -0.0005 sr^{-1} to ensure that spectra are not significantly negative in the ultraviolet range.
- Mean R_{rs} intensity in range (800-900 nm) ≥ -0.0005 sr^{-1} to remove spectra that are significantly negative in this range of NIR region.
- Maximum R_{rs} intensity ≤ 0.03 sr^{-1} to remove spectra affected by sun glint and foam.
- In order to exclude the measurements effected by direct solar transmittance, ship shadows and reflections, the ship log data, i.e, the ship heading from North, and solar azimuth angles were used to maintain the viewing relative azimuth angle between sensors and the sun in the range ($90 < \Delta\Phi < 180$).

In addition to the above-mentioned criteria, the in-situ R_{rs} spectra were excluded if the sun zenith angle $> 65°$. The in-situ spectra that passed the above criteria were averaged over the spectral response of the MSI acquired from (https://earth.esa.int/web/sentinel/user-guides/sentinel-2-msi/document-library/). The processed in-situ R_{rs} spectra after weighted averaged over the spectral response of the MSI, are shown in Fig. 4.

In this study, bidirectional water correction was not applied for neither in-situ nor satellite-derived R_{rs} data [7], [39]. This is because i) the bidirectional contribution from water is generally small [39], and ii) we wanted to minimize the additional uncertainties that could be associated with the correction (e.g., glint, boat disturbances, sky reflectance, etc.). It should be noted that the Acolite DSF method does not take into account the bidirectional correction, so a direct comparison is not possible [40].

2) Match-ups selection: In this work, the comparison between in-situ R_{rs} and atmospherically corrected R_{rs} is carried out for S2 MSI images only; the nearest L8 overpasses have high zenith angles ($> 70°$) and are therefore not included in the match-up analysis. For a match-up selection, R_{rs} data were taken from re-sampled S2 images over a window of 3×3 R_{rs} pixels (equivalent to 180×180 m) centered around the in-situ location [10], [44]. A median value of R_{rs} pixels that passed the quality flags was selected to best represent a match-up. To prevent overlap between the match-ups, the distance between the central pixel of the 3×3 pixels window should be greater than 180 m

This article has been accepted for publication in IEEE Transactions on Geoscience and Remote Sensing. This is the author's version which has not been fully edited and content may change prior to final publication. Citation information: DOI 10.1109/TGRS.2022.3228393

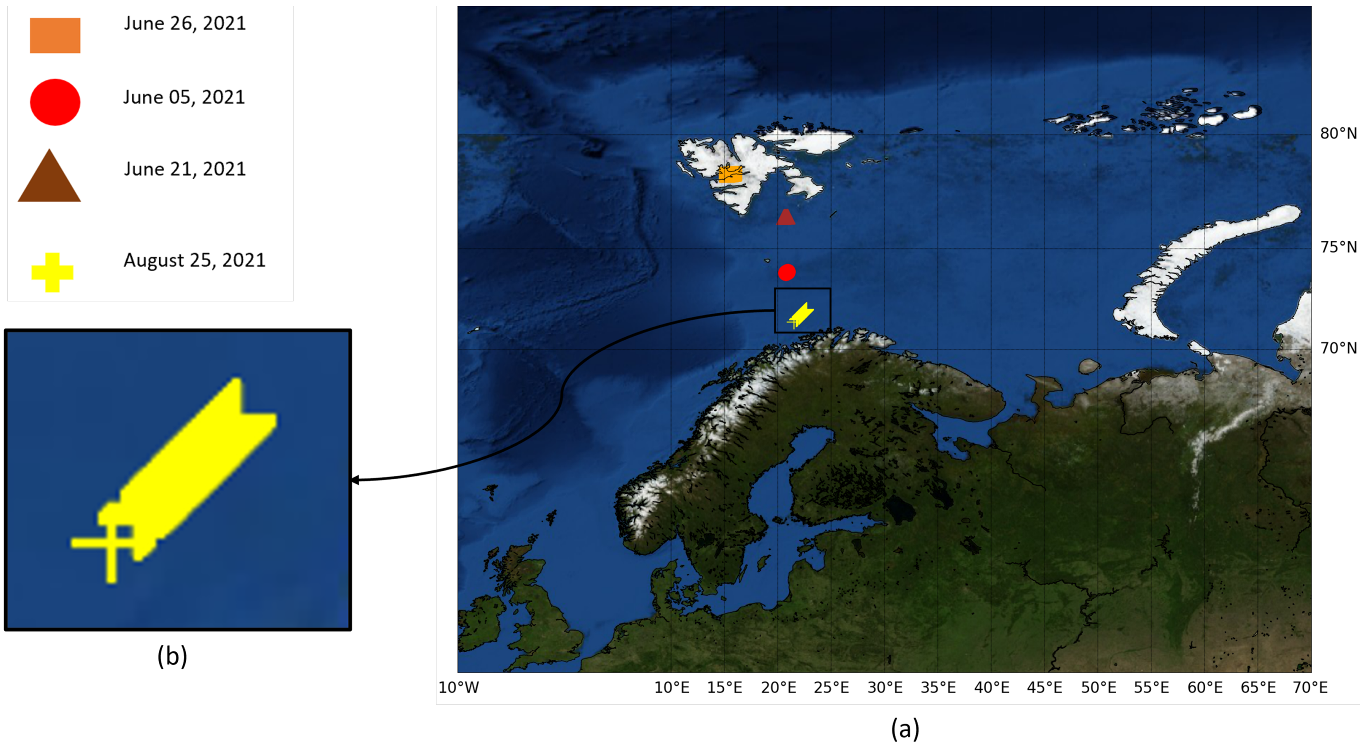

Fig. 2: Geographic location of (a) the in-situ radiometric spectra that passed the quality control procedures and near-coincident with Sentinel-2A/B overpasses, are represented by different legends. b) closeup showing a matching transect. (For interpretation of the references to colour in this figure legend, the reader is referred to the web version of this article.)

TABLE I: Sentinel-2A/B MSI and Landsat-8 OLI spectral bands and spatial characteristics [9], [15], [24], [41]–[43].

	Landsat-8 OLI		**Sentinel-2A/B MSI**	
Swath/field of view	**180 km/15°**		**290 km/20.6°**	
Altitude	**705 km**		**786 km**	
Bands	**Wavelength [nm] (Band center)**	**Spatial Resolution [m]**	**Wavelength [nm] (Band center)**	**Spatial Resolution [m]**
Coastal aerosol	435–451 (443)	30	433–453 (443)	60
Blue	452–512 (482)	30	458–523 (490)	10
Green	525–600 (561)	30	543–578 (560)	10
Red	636–673 (655)	10	650–679 (664)	10
Red edge			698–793 (705)	20
			733–748 (740)	20
			773–793 (783)	20
NIR	851–879 (865)	30	785–900 (842)	10
			855–875 (865)	20
SWIR	1566–1651 (1609)	30	1565–1655 (1610)	20
SWIR	2107–2294 (2201)	30	2100–2280 (2190)	20

from the central pixel of the preceding match-up. Pixels contaminated by adjacent land, cloud cover, and sun glint were masked using the AC pixel quality flags in the default settings. The spectra were discarded if R_{rs} value higher than 1 or less than $-0.0005\,\mathrm{sr}^{-1}$ at any wavelength [7]. In addition, a match-up was discarded if the number of valid pixels were < 5 or failed to pass the homogeneity test, i.e, coefficient of variation (CV) < 0.15 for bands at 443, 492 and 560 nm [30].

Though we have collected continuous ship-based data from the year 2021, allowing a time window of $\pm$ 3 hours [30], we achieved four cloud-free S2 match-up scenes. This is due to the frequent cloud coverage and the disregarding of any possible errors in the in-situ R_{rs} measurements to ensure high quality data. After matching in-situ R_{rs} measurements collected along the navigation of the ship to S2 overpasses, we extracted 277 match-up pixels for Acolite, compared to 226 and 338 match-up pixels for the Polymer and C2RCC algorithms, respectively. The different numbers of match-ups resulted from the difference in default quality flags used for the individual AC (non-water pixels such as clouds, shadows, and land).

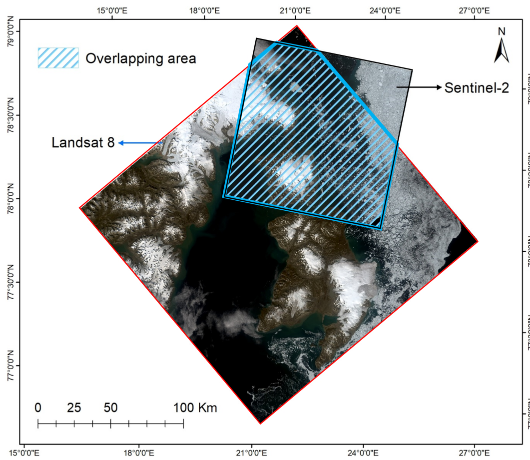

Fig. 3: An example of a near-simultaneous overpasses of OLI-MSI over Longyearbyen. The red frame shows the OLI image footprint, and the black frame represents the MSI image footprint. The inter-comparisons are made for the overlapping region (pixels) represented by a blue frame. The time-difference between the two overpasses is 15 minutes. (For interpretation of the references to colour in this figure legend, the reader is referred to the web version of this article.)

C. OLI-MSI R_{rs} inter-comparisons

The core part of the present study is the spectral harmonization of OLI-MSI R_{rs} products (Fig. 1). Details about ρ_t inter-comparisons are provided in Appendix A-A. An example of near-simultaneous OLI-MSI overpasses over the study region is given in Fig. 3.

For R_{rs} inter-comparisons, we have considered near-simultaneous overpasses with a time difference of ±30 minutes with low or no cloud cover. The differences in data products under such a narrow time window, to a large extent, can be attributed to differences in the sensors' absolute radiometric responses [10], [27]. In this study, the OLI-derived data products are considered as the reference to assess MSI products [9] due to the OLI's improved signal-to-noise ratio (SNR) [45] and radiometric calibration [46]. The R_{rs} inter-comparisons were carried out for the water pixels in the common bands only, depicted in Table. IV.

To minimize random noise and artifacts, a median value of valid water pixels (non-masked) over 6 × 6 and 3 × 3 pixels window were extracted from 30 m L8, and 60 m re-sampled S2 images, respectively. The whole window was excluded from inter-comparison if the CV across the window was greater than 50%. In addition, spectra with $R_{rs}(\lambda) > 0.03$ (sr^{-1}) and $R_{rs}(865\text{nm}) > 0.001$ were removed from the inter-comparison [7], [47]. These modified thresholds were determined by analyzing both the in-situ (Fig. 4) and satellite-derived R_{rs} spectra from a wide region of the Barents Sea, i.e., the open waters, coastal waters, and marginal sea-ice region. Some erroneous or non-realistic spectra might have occurred from the underestimation/overestimation of the path reflectance, cloud shadow, sun-glint, or sub-pixel contamination due to sea-ice. The masking thresholds adopted in the present study allow the retrieved spectra to converge, provide a realistic water spectrum, and match the spectral shape of in-situ measurement. To avoid over correction by AC processors, the R_{rs} intensity should be larger than -5×10^{-4} sr^{-1} in the range 800 nm to 900 nm [47]. In addition, we have experimented with different flagging criteria mentioned in the previous works [9], [10], [28] to improve the inter-sensor spectral consistency. For example, to minimize the bidirectional effects, we computed the view zenith angle per band and performed the inter-comparisons for the pixels with the view zenith angles (VZA) within the ±5° range [10]. Similarly, we exclude inter-comparison scenes with solar zenith angle (> 65°) [9]. To ensure similar environmental and aquatic conditions and acquire an adequate amount of inter-comparison pixels, we experimentally analyzed the effect of time-gap (10 − 60 minutes) on the spectral difference between S2 and L8 overpasses [10], [27], [28]. To avoid the large computational burden, inter-comparison pixels were selected within a window of 180 × 180 and 90 × 90 for L8 and S2 images, respectively, around the central pixel in the shared region.

D. Proposed Bandpass adjustment model

The architecture and systematic system diagram illustrating the main components of the proposed BA method are given in Fig. 5. In the following subsections, we further explain the architecture and training process following the R_{rs} inter-comparisons described in section. III-C.

1) Reflectance adjustment of Sentinel-2 observations: To harmonize the spectral domains of OLI L8 and MSI S2, using L8 R_{rs} as a reference, the proposed BA model accounts for the differences in SRF of these sensors. The BA model is trained to perform pixel-by-pixel transformation from S2 derived R_{rs} to L8 derived R_{rs}. Note that, in this work following the study [9], the BA model was trained for combined S-2A and S-2B sensors. The trained model was then used to predict L8 OLI equivalent R_{rs} for those derived from S2 MSI. Following that, the OLI R_{rs} and the adjusted MSI R_{rs} (MSI*) are then merged. The framework shown in Fig. 1 gives an overview of the workflow we used to train our model for performing the spectral harmonization, i.e., the transformation of MSI S2 R_{rs} products into the spectral domain of OLI L8. In the current work, we have used the four visible bands common to S2 and L8, i.e., Band-1 (ultra-blue/coastal aerosol), Band-2 (blue), Band-3 (green), and Band-4 (red). The spectral adjustment is performed individually for each of these bands [9], [10]; however, for better generalization of the model, we have increased the number of input features [48]–[50]. The R_{rs} product, the normalized R_{rs} in the range between 0 and 1, and the R_{rs} in log-scale, were given as an input to the network. This means that the network has three input features and one output. Fig. 5 illustrates a schematic block diagram of our developed BA model.

2) Hyperparameters: The selection of a suitable set of connecting weights, the depth of the network, the number of neurons in each hidden layer, batch size, activation

This article has been accepted for publication in IEEE Transactions on Geoscience and Remote Sensing. This is the author's version which has not been fully edited and content may change prior to final publication. Citation information: DOI 10.1109/TGRS.2022.3228393

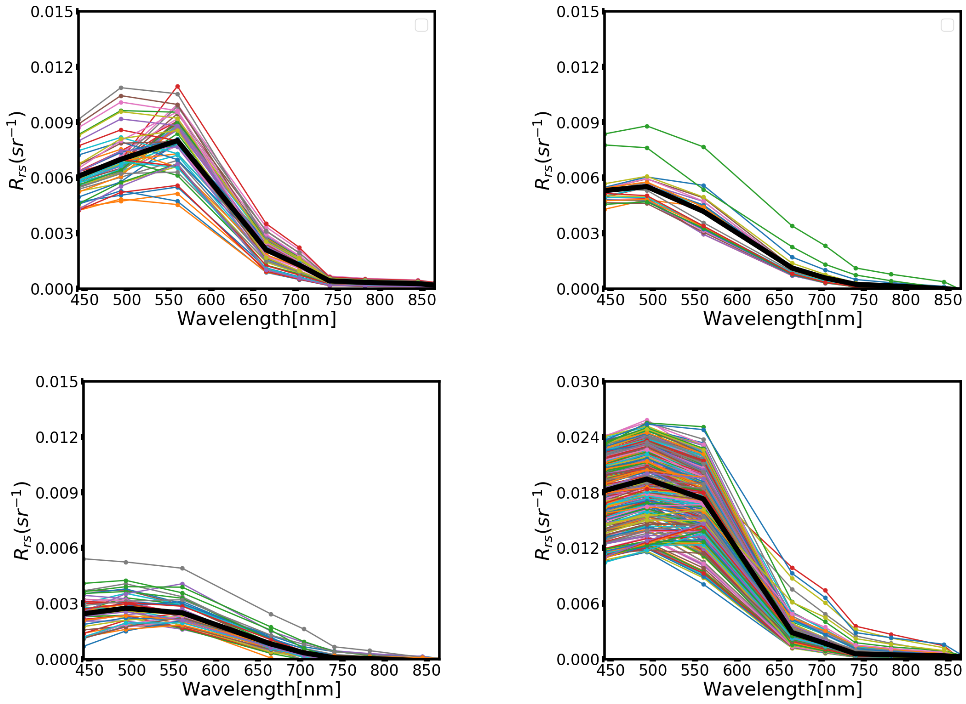

Fig. 4: In-situ R_{rs} spectra of the four match-ups with a time-difference of ± 3 hours with Sentinel-2 A/B overpasses, convoluted to the S2-MSI spectral bands using the Sentinel-2 A/B Spectral Response Functions S2-SRFs (version 3.0). The solid black lines refer to the mean R_{rs} spectra.

function, learning rates, and regularization all play a crucial role in estimating any measurable function between the input and output vectors [51]. In this regard, different designs of the MLP were implemented, and the one with three hidden layers having 25, 15, and 10 neurons and tanh activation function is found to be the best performer based on the validation error (Table. II). In the current study, a mini-batch gradient descent method is used to compute the gradients of the cost function with respect to the weights w and biases b of the network. After the activation function, the batch normalization (BN) was applied after each hidden layer for regularization [52]. The BN minimized the internal covariance shift in the data distribution in the layers and speed up the learning process [52]. The output of the model is a single value of R_{rs} (MSI*), which is passed to the loss function. The difference between the adjusted MSI R_{rs} equivalent to the OLI one (MSI*) and the true value of R_{rs} OLI is minimized by the optimization process using the back propagation algorithm. In this work, the loss function is based on the root mean square log difference (RMSLD) along with the ℓ_2 norm on the weights and the biases, w and b:

$$L = \sqrt{\frac{1}{N}\sum_{i=1}^{N}\left(\log_{10}(z_i) - \log_{10}(\widehat{z_i})\right)^2 + \lambda_1 \ell_2(W,b)} \qquad (1)$$

where $\widehat{z_i}$ is the predicted value and z_i is the corresponding ground-truth value, N is the total number of samples, and λ_1 is a hyper-parameter used to assign relative importance to the second term.

The batch size is fixed to 64 samples, and the initial learning rate η_0 was set at 0.0075, which decreases by 5% after every 100 epochs. The choice of these two hyper-parameters was made based on the training and validation errors. For faster convergence of the model, the weights and biases were initialized using the Xavier method [53]. The parameters/hyper-parameters are summarized in Table. II.

3) Experimental Setup: To evaluate the performance of the proposed BA model, the inter-comparison R_{rs} pixels were randomly split into 80% training and 20% testing samples using 5-fold cross-validation. The training samples in each split are subdivided into training and validation (70% and 30%) samples. Using the training data only, the BA model is trained for 5000 epochs in each split. To avoid overfitting and better tuning of the hyper-parameters, during the training process, the BA model with weights and bias terms having minimum validation error is utilized to estimate R_{rs} (MSI*) on the unseen data. The BA model is developed in Tensor Flow, Python [54].

The linear regression model is also implemented in a Python environment and has been utilized in different studies for the spectral-adjustment [9], [11], [15]. Using L8 as reference data (Eq.(2)), the regression coefficients are calibrated by combining training and validation data.

$$Y(\lambda_i) = a_0 R_1(\lambda_i) + a_1 R_2(\lambda_i) + a_2 R_3(\lambda_i) + b \qquad (2)$$

Where λ_i represents band number of S2 and L8 respectively. Here a_0, a_1, a_2 and b are regression coefficients. These coefficients are obtained for each pixel by minimizing the spectral difference between S2 and L8 R_{rs} products. Here

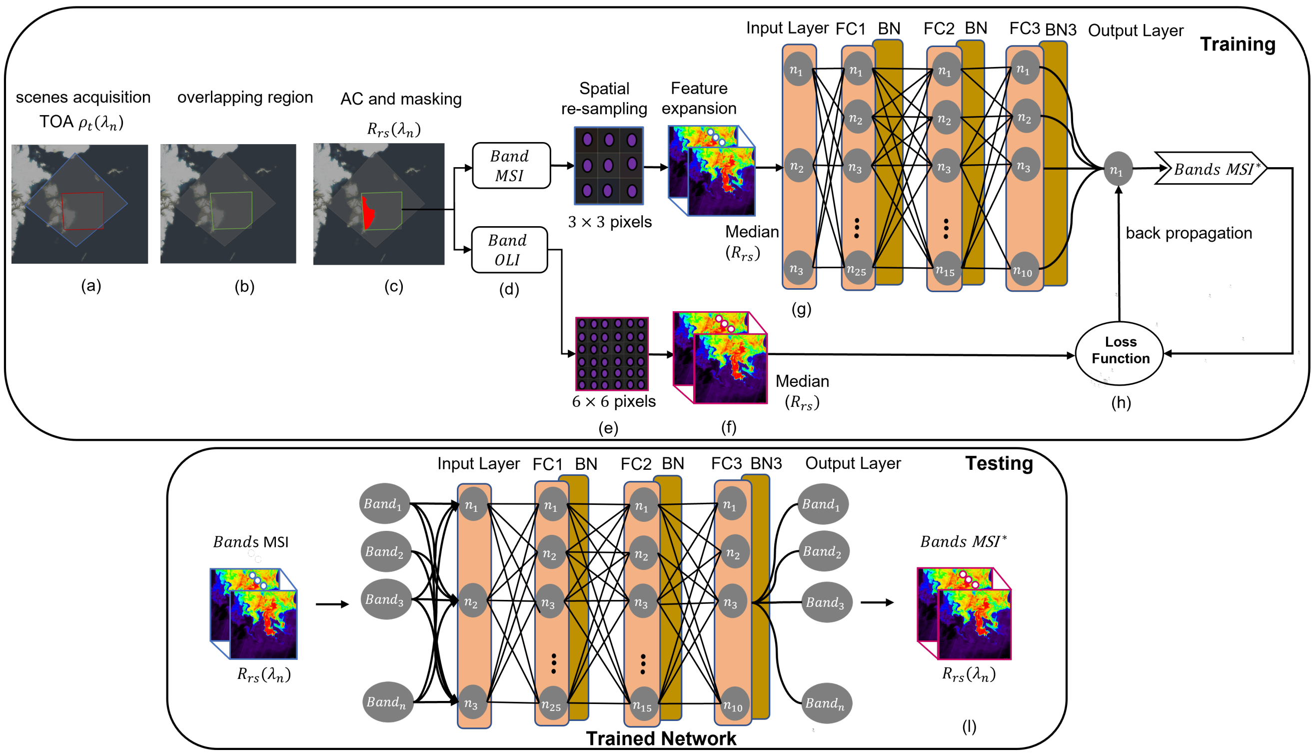

Fig. 5: The proposed framework for spectral bandpass adjustment. a) L8 and S2 scenes acquisition at the TOA with a time difference of < 30 minutes overpasses the same region (Appendix A-A). b) Overlapping region between near-simultaneous S2 and L8 scenes. c) The TOA reflectance (ρ_t) are corrected for atmospheric effects to extract water surface R_{rs}. Pixels affected by land and cloud are masked (section III-C). d) L8 and S2 bands with non-water R_{rs} pixels flagged. e) Spatial re-sampling of water R_{rs} pixels (section III-C). f) Feature expansion and flagging erroneous pixels (section III-C). g) Input to the Fully Connected (FC) neural network with an input layer, three hidden layers and an output layer (section III-D). The hidden layer blocks consist of an FC and Batch Normalization (BN) layers. h) Network loss computation and weights update (section III-D2) and l) Predicted OLI (MSI*) R_{rs} products for each band from that of MSI R_{rs} products.

TABLE II: Parameters of the proposed model for spectral harmonization.

Parameters	Value/Selection	Description
Layers	5	input-layer, 3 hidden-layers, output-layer
Number of Neurons	3,25, 15, 10, 1	
Weight Initialization	Xavier	
Activation Function	tanh	
Learning Process	mini-batch gradient descent	
Loss Function	RMSLE	
Regularization	Batch-Normalization, L2-norm and Early stopping	
Optimizer	Adam	initial learning rate=0.0075
Batch-size	64	

R_1, R_2, R_3 represents the S2 derived R_{rs} products, the normalized R_{rs} product in the range between 0 and 1, and the R_{rs} product in log-scale.

E. Evaluation Metrics

The differences in the in-situ and MSI derived R_{rs} products (section IV-A) and R_{rs} between L8 and S2 (section IV-B), are expressed in terms of the root mean square difference (RMSD), the root mean square difference in log scale (RMSLD), the median absolute percentage difference (MAPD), the median relative percentage difference (MRPD) and the coefficient of determination (R^2). These metrics are represented by Eqs.(3), (4),(5), (6), and (7), respectively.

$$RMSD = \sqrt{\frac{1}{N_t}\sum_{i=1}^{N_t}(X_i - Y_i)^2} \tag{3}$$

$$RMSLD = \sqrt{\frac{1}{N_t}\sum_{i=1}^{N_t}\left(\log_{10}(X_i) - \log_{10}(Y_i)\right)^2} \tag{4}$$

$$MAPD = 100\% \times median\left(\frac{|X_i - Y_i|}{|Y_i|}\right) \tag{5}$$

$$MRPD = 100\% \times median\left(\frac{X_i - Y_i}{Y_i}\right) \tag{6}$$

$$R^2 = 1 - \frac{\sqrt{\sum_{i=1}^{N_t}(Y_i - X_i)^2}}{\sqrt{\sum_{i=1}^{N_t}(Y_i - \bar{X})^2}} \quad (7)$$

where X_i represents S2 derived R_{rs} and ρ_t products (sections IV-A, A-B and IV-B). Y_i represents in-situ R_{rs} or L8 derived R_{rs} and ρ_t products (A-B and IV-B). Here, N_t, indicates number of test samples. $\bar{X} = \frac{1}{N}\sum_{i=1}^{N} X_i$ is the mean R_{rs} value and $median$ is the median operator.

IV. Results and Discussion

The results are presented in two subsections. Subsection IV-A shows comparison of Acolite, C2RCC and Polymer-retrieved R_{rs} with the in-situ data (match-ups). The performance analysis of these AC processors is described in two settings: i) an assessment of each processor independently and ii) an evaluation of common data (considered as valid R_{rs} pixels by all the AC processors) among AC processors. The latter allows performance assessment using identical match-ups, while the former allows an assessment of their practicality, including the masking of non-water and erroneous pixels.

The inter-comparison of OLI-MSI R_{rs} products (before and after spectral BA) are illustrated in subsections IV-B, and IV-C respectively.

A. AC evaluation

To provide a straightforward assessment of the performance of an individual processor, the match-ups for R_{rs} at 443, 492, 560, and 665 nm derived from the Acolite, the C2RCC, and the Polymer using MSI data are shown in Fig. 6 (see also Table. III for error matrics).

In general, the scatter plots in Fig. 6 show that Acolite tends to overestimate R_{rs}, whereas the opposite holds true for C2RCC and Polymer except the red band; the degree of over-or underestimation varies depending on the spectral band (improving or degrading from the blue to red) and the magnitude of R_{rs}.

For Acolite, the overestimation of R_{rs} values decreases from the 443 nm to the 560 nm band. The R_{rs} estimates are close to the 1:1 line at 560 nm (Fig. 6 a3). However, R_{rs} at the 665 nm band are significantly above the in-situ observations.

For C2RCC and Polymer, while significant underestimates are observed at higher R_{rs} values at 443 nm, the degree of underestimation reduces at 492 and 560 nm (Figs. 6 b1-3). At 665 nm, the R_{rs} values are dispersed around the 1:1 line irrespective of the in-situ R_{rs} range but bias is minimal (Fig. 6 b4 and c4; Table. III).

Overall, Acolite and C2RCC showed the smallest biases from the in-situ R_{rs} measurements with an averaged RMSD of 3.33×10^{-3} and 3.49×10^{-3}, respectively (Table. III). In contrast, the Polymer derived R_{rs} products have a higher error with an RMSD of 4.20×10^{-3}. The Acolite derived R_{rs} exhibits better performance with reduced RMSD of 5% and 20% compared to C2RCC and Polymer. According to the other criteria, including MAPD and RMSLD, Acolite performed moderately better in the 442-492 nm bands with MAPD=21% and RMSLD=0.154, best in the 560 nm band with MAPD < 10% and RMSLD=0.079, however, high uncertainties were found in the 665 nm band with MAPD=63% and RMSLD=0.234. At 665 nm, Acolite estimates are significantly higher than the in-situ R_{rs} with MAPD=49% greater than C2RCC-retrieved R_{rs}. The MRPD further corroborates the limited performance of Acolite in the 665 nm band, and better performance in the 443-560 nm bands compared to C2RCC and Polymer. In the 665 nm band, C2RCC is the top performer with MAPD=~ 8% and RMSD=11% less than Polymer.

It is noted that consistent positive or negative biases are evident across all the processors. For example, MRPD is always positive for Acolite, but it is negative for all bands for C2RCC and Polymer. The higher estimates of R_{rs} relative to in-situ values from the blue to green bands using the Acolite DSF scheme are consistent with those from previous studies [6], [55]. The overestimation of Acolite derived R_{rs} is likely attributed to the underestimation of aerosol loads or differences between the estimated AOT and the true aerosol properties [7], [8]. This is partly explained by the averaged AOT of ~ 0.12 at 550 nm derived from Acolite in the present study. The averaged AOT of 0.12 illustrate moderate aerosol loads compared to AOT-550 nm measured over AERONET stations in [56], [57]. In contrast, Polymer and C2RCC estimates are significantly lower than the in-situ and Acolite-derived R_{rs}. Similar performance for Polymer and C2RCC (underestimating higher R_{rs} values) are reported in [58] and [59]. This is attributed to the discrepancy between the in-situ water reflectance and a water reflectance model implemented in Polymer processor (F. Steinmetz, personal comm.). For C2RCC, while the exact cause of the discrepancy is unknown, the limited performance may be due to the difference between optical properties of the training sets used in C2RCC-nets, which is not necessarily representative of the Barents Sea waters. This hypothesis is supported by Kratzer et al. [60], which improved the performance using the locally tuned C2RCC-nets for the Baltic Sea (10% improvement in the RMSD).

Our discussion on the performance of the three processors remains the same, using either all valid data available for an individual processor or common data for all of the processors. Using the common match-ups between the three AC processors, the MAPD improved by < 1% for Acolite, > 3% for C2RCC and <6% for Polymer. Similarly, all processors show improved RMSLD and MRPD. For example, the RMSLD reduces by 10% for Acolite retrieved R_{rs} data. No significant difference is observed in the RMSD. In this study, none of the AC schemes meet the 5% retrieval accuracy requirement across the blue-green bands [61], except Acolite at the 560 nm band for the common data. It should be noted that this requirement is typically valid for clear and oligotrophic waters where optical properties are exclusively dominated by phytoplankton (Chl-a <1 mg m^{-3}) [62]. Larger uncertainties have been observed in the turbid waters in the blue-green bands, 25 to 60% in [8], 23 to 42% in [39], and 40 to 60% in [7].

This article has been accepted for publication in IEEE Transactions on Geoscience and Remote Sensing. This is the author's version which has not been fully edited and content may change prior to final publication. Citation information: DOI 10.1109/TGRS.2022.3228393

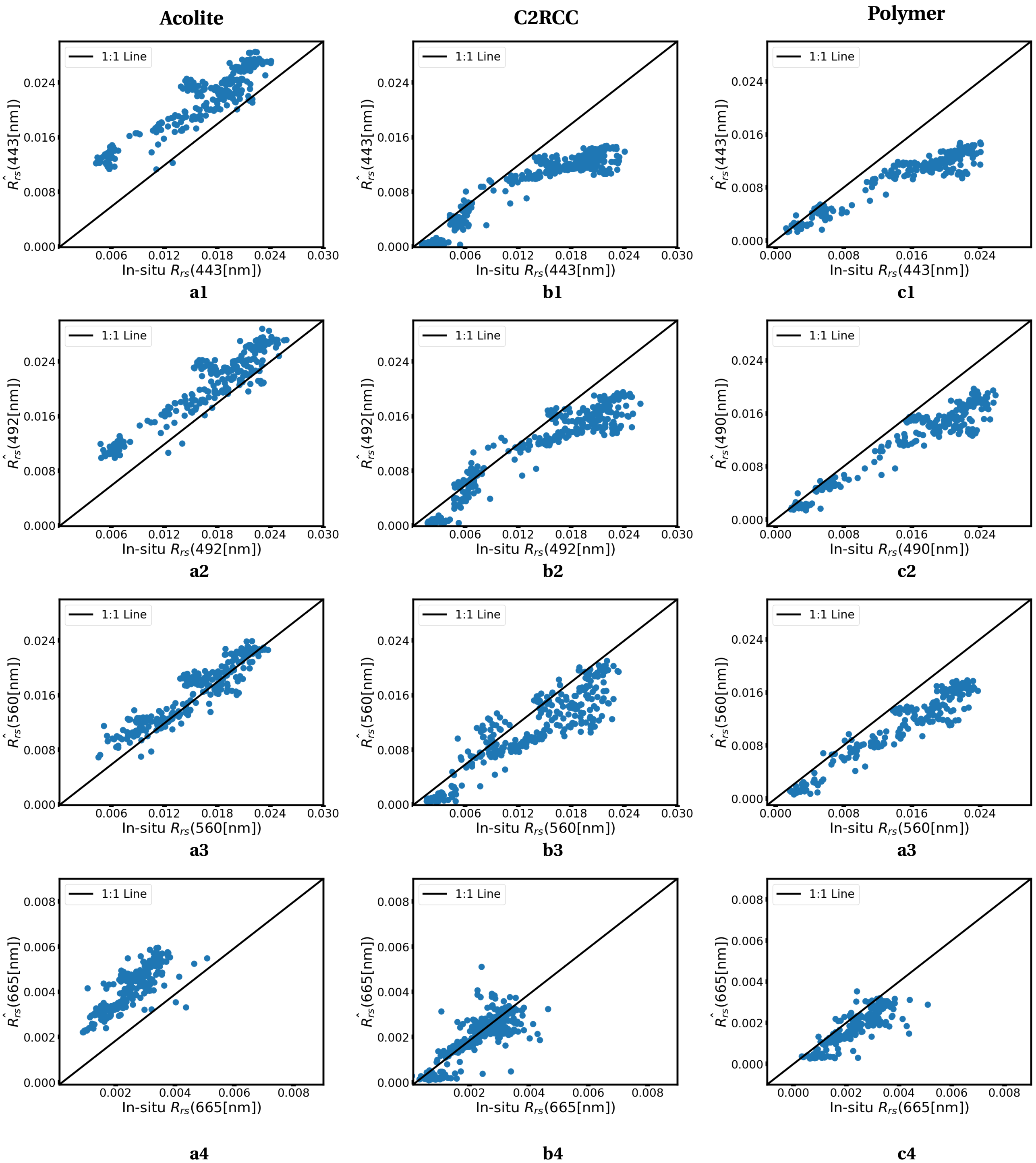

Fig. 6: Overall performance comparison of AC processors against the in-situ data in the four visible bands using data acquired from the S2 MSI. Detailed statistical metrics are available in Table. III. The solid black lines are the 1:1 match.

B. Spectral bandpass adjustment for R_{rs}

The previous section indicated that the R_{rs} products retrieved via Acolite have minimum spectral differences from the in-situ R_{rs} compared to the other AC processors tested in the present study. As mentioned in section I, the key objective of this study is to develop a practical method for merging MSI and OLI images in terms of R_{rs} products. Before doing so, OLI-MSI R_{rs} products retrieved via Acolite, Polymer and C2RCC were examined. Our inter-comparison results show that S2 and L8-derived R_{rs} products retrieved via Acolite have a minimum difference compared to the other AC processors, as illustrated by the evaluation metrics in Table. IV and Appendix (Table. B.1). In the following section, the Acolite derived OLI and MSI R_{rs} products are used for spectral harmonization (see Figs. 1 and 5).

The relationships between the OLI and MSI-derived R_{rs}

This article has been accepted for publication in IEEE Transactions on Geoscience and Remote Sensing. This is the author's version which has not been fully edited and content may change prior to final publication. Citation information: DOI 10.1109/TGRS.2022.3228393

TABLE III: Match-ups of remote sensing reflectance derived from Acolite, C2RCC, and Polymer AC processors against the in-situ dataset for all the valid data. For each band, the best results are shown in bold.

Bands	N	RMSD (10^{-3} sr^{-1})	RMSLD	MAPD	MRPD
All data					
443 nm Acolite	277	**5.44**	**0.182**	**25.79**	**25.79**
492 nm Acolite	277	**3.89**	**0.126**	**16.94**	**16.78**
560 nm Acolite	277	**2.31**	**0.079**	**9.840**	**5.690**
665 nm Acolite	277	1.72	0.234	63.40	63.40
443 nm C2RCC	338	5.61	0.297	33.91	-33.91
492 nm C2RCC	338	4.11	0.252	22.08	-21.19
560 nm C2RCC	338	3.62	0.246	24.28	-22.46
665 nm C2RCC	338	**0.65**	0.257	**14.11**	**-10.11**
443 nm Polymer	226	6.73	0.203	37.09	-36.99
492 nm Polymer	226	4.93	0.140	24.09	-24.06
560 nm Polymer	226	4.43	0.191	25.92	-25.92
665 nm Polymer	226	0.74	**0.205**	22.30	-21.92
Common data					
443 nm Acolite	167	**5.30**	**0.158**	**24.50**	**24.50**
492 nm Acolite	167	**3.86**	**0.109**	**16.01**	**16.01**
560 nm Acolite	167	**2.26**	**0.071**	**9.16**	**4.940**
665 nm Acolite	167	1.71	0.233	62.94	62.94
443 nm C2RCC	167	6.63	0.188	33.25	-33.25
492 nm C2RCC	167	4.88	0.121	20.22	-19.93
560 nm C2RCC	167	4.33	0.133	21.09	-19.71
665 nm C2RCC	167	**0.64**	**0.103**	**12.33**	**-8.560**
443 nm Polymer	167	7.14	0.210	37.35	-37.35
492 nm Polymer	167	5.30	0.134	24.33	-24.33
560 nm Polymer	167	4.78	0.144	24.18	-24.18
665 nm Polymer	167	0.75	0.138	21.65	-20.32

products retrieved by applying Acolite to ρ_t TOA (presented in Appendix A-B) are shown in Fig. 7 (a1-a4). Also shown is the relationship between OLI R_{rs} and MSI^* R_{rs} derived from MSI after spectral BA OLS regression (Fig. 7 b1-b4) and the NN based model proposed in the present study (Fig. 7 c1-c4) for the common visible bands.

Without BA, the average differences in R_{rs} products retrieved via Acolite are estimated to range from 6 to $\sim 12\%$ (Table. IV). Visual inspection of the scatter plots in Fig. 7 (a1-a3) and comparison of the MRPD show that OLI-derived R_{rs} products are higher in magnitude than that of MSI-derived R_{rs} products from blue to green bands. These findings are in accordance with [10]. The highest bias is found in the R_{rs}(665 nm) products with MRPD of $\sim -11\%$ and RMSLD=0.096. The worst performance in the red band is likely due to the lower water reflectance measured at higher wavelengths in oceanic waters [7]. In addition, with reference to Table. I and the study [63], the red bands of L8 and S2 have the minimum percentage of overlap in the SRF and a larger difference in the central wavelengths, which also contributes to the higher bias. Likewise Acolite, C2RCC R_{rs}(665 nm) products also achieved a worse performance (Table. B.1). Comparing all the evaluation metrics, the minimum spectral difference is achieved in the 561 nm products with MAPD=6.58% and $R^2 = \sim 0.95$.

After applying the proposed spectral BA, the difference was significantly reduced from $< 10\%$ to $< 3\%$, demonstrating the effectiveness of the proposed approach (Table. IV). Comparing the performances of the BA methods and considering MAPD and RMSLD as performance measures, on average, the proposed BA approach reduced MAPD and RMSLD by $\sim 2.8\%$ and $\sim 41\%$, compared to the $\sim 1.1\%$ and $\sim 33\%$ improvement made by the OLS regression model. In addition, the proposed BA approach has achieved reduced RMSD, 8% less than the OLS regression model. Fig. 7 further demonstrates the outperformance of the proposed BA model over the OLS model. This is because the proposed BA model takes advantage from the capability of a deep neural network to accurately learn and model the nonlinear problem (transformation of MSI-R_{rs} to that of OLI-R_{rs}), while preserving the spectral properties of the two satellite sensors. It can been seen that the OLS model underestimates the higher R_{rs} values ($R_{rs} > 0.018$ in Fig. 7 (b1-b3) and $R_{rs} > 0.005$ in Fig. 7(b4)). In contrast, R_{rs} using the proposed BA model is less affected by the magnitude of R_{rs} values, highlighting the generalizability of the model which is partially due to the extension of input feature vectors (see Fig. 5 in section III-D). Our results show that the OLS model can reduce the reflectance difference to only a few degrees. It is possible that the OLS transformation coefficients may not be suitable to solve nonlinear harmonization problems where different water types may exist. Comparing all the bands, the highest improvement is achieved in the R_{rs}(482 nm) products, while the lowest is in the R_{rs}(561 nm) products by both the BA methods. Overall, our analysis indicates that the proposed BA model has achieved better performance in the spectral adjustment for S2 MSI data to fit L8 OLI data with a considerable decrease in the RMSD (30%). The RMSD and median difference of $\sim 5 \times 10^{-4}$ and 3.53×10^{-5} sr^{-1}, respectively, are within the acceptable uncertainties for ocean colour products, i.e., 5×10^{-4} [64]. The improvement in spectral alignment between OLI-MSI R_{rs} products is evident for all the bands in Table. IV.

This article has been accepted for publication in IEEE Transactions on Geoscience and Remote Sensing. This is the author's version which has not been fully edited and content may change prior to final publication. Citation information: DOI 10.1109/TGRS.2022.3228393

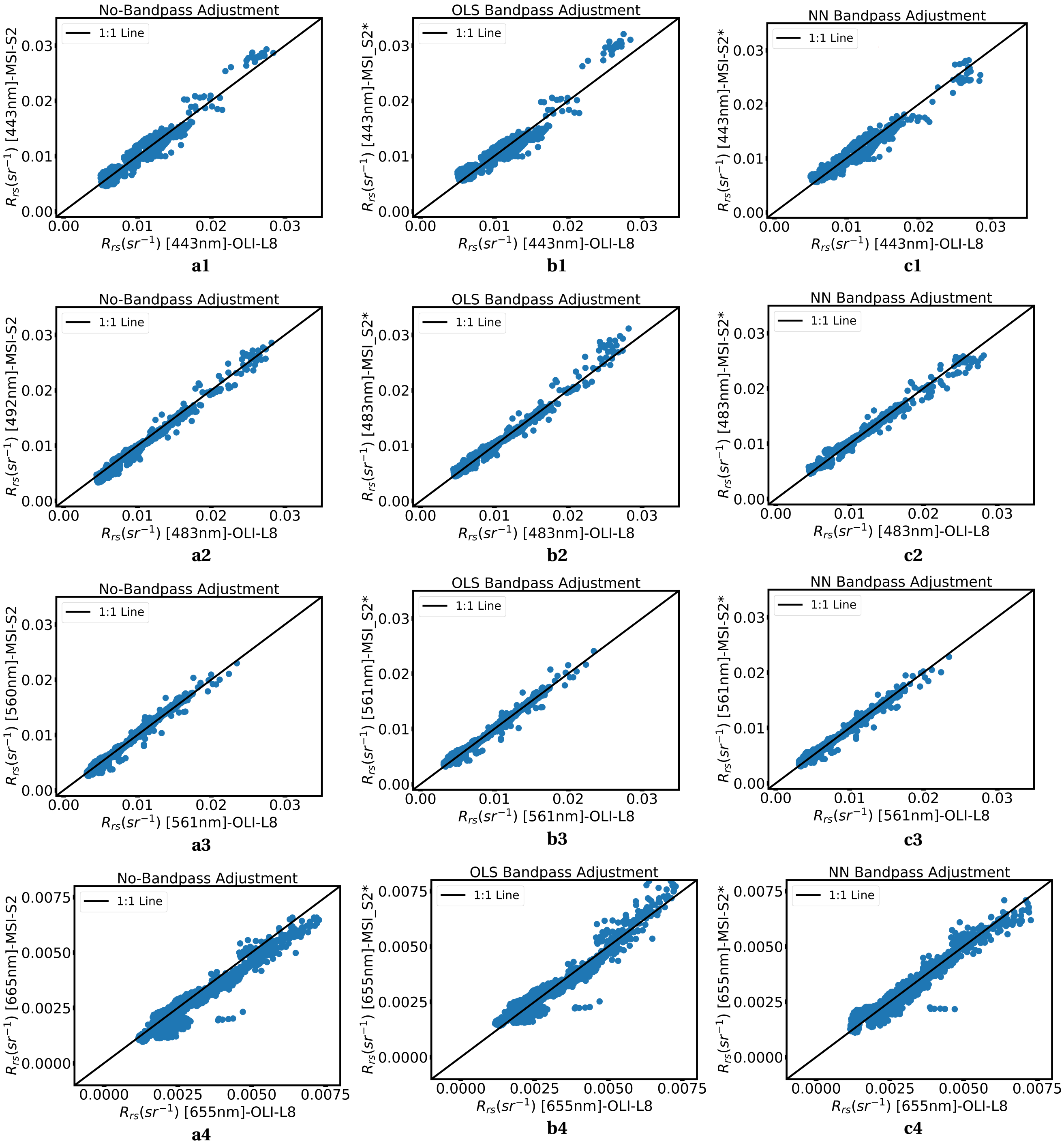

Fig. 7: Inter-comparison of R_{rs} products for OLI and MSI processed via Acolite. Detailed statistical metrics are available in Table. IV.

C. Further evaluation of proposed BA method

To ensure the performance of the proposed BA method, we use additional scene images of OLI and MSI that are independent relative to those used in the previous section. Fig. 8 shows an example of near-simultaneous OLI and MSI image pairs acquired over the study site on July 24, 2019. It can be seen that the study site contains both coastal and open ocean waters.

1) Comparison of R_{rs} products: In Fig. 9, OLI-derived R_{rs} products alongside with MSI products retrieved via Acolite, C2RCC and Polymer are shown. Overall, the Acolite scheme produces MSI-derived R_{rs} similar to those of OLI, as compared to C2RCC and Polymer. The fine spatial details of in-water optically active components are noticeable in Acolite-processed R_{rs} products in OLI-MSI images at nearly the same location. C2RCC and Polymer schemes have also captured the spatial variations in the R_{rs} products, however,

TABLE IV: Inter-comparison of OLI-MSI R_{rs} products for N=8500 pixel pairs extracted from near-simultaneous 42 OLI and 71 MSI image pairs. The best results are shown in bold.

Method	RMSD (10^{-4} sr^{-1})	RMSLD	MAPD	MRPD	R^2
	Coastal aerosol (443 nm)				
Proposed NN	**8.41**	**0.035**	**4.999**	**0.015**	**0.879**
OLS	8.62	0.039	6.319	0.472	0.865
No Bandpass Adjustment	9.120	0.048	8.056	-3.558	0.846
	Blue (482 nm)				
Proposed NN	**4.94**	**0.028**	**2.841**	-0.449	**0.964**
OLS	5.79	0.032	5.074	**-0.085**	0.95
No Bandpass Adjustment	9.380	0.057	6.679	-6.554	0.869
	Green (561 nm)				
Proposed NN	**4.29**	**0.037**	**4.5**	-1.213	**0.974**
OLS	4.47	0.038	5.337	**-0.289**	0.972
No Bandpass Adjustment	6.16	0.058	6.586	-5.0	0.946
	Red (665 nm)				
Proposed NN	**2.69**	**0.053**	**9.705**	**0.693**	**0.895**
OLS	3.20	0.063	12.084	1.533	0.852
No Bandpass Adjustment	4.46	0.096	11.917	-10.775	0.714

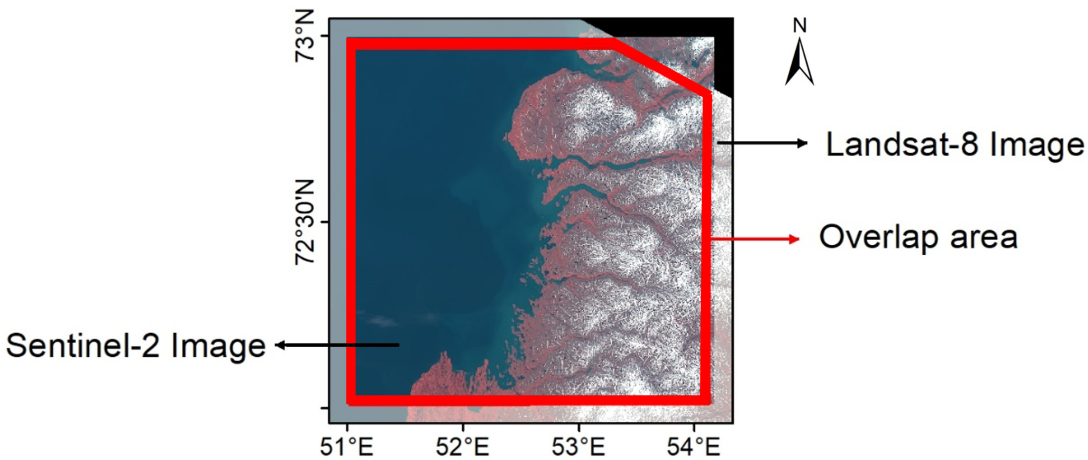

Fig. 8: OLI and MSI images acquired over the study region with a time-difference of 17 minutes. The OLI and MSI scenes were acquired on July 24, 2019.

a larger difference is observed in the magnitude of estimated R_{rs} in the two datasets, especially close to the coast, as illustrated by the ellipses in Fig. 9. Furthermore, the masking of clouds and land in Acolite-processed products is consistent, whereas C2RCC and Polymer have masked larger areas in MSI images than OLI.

It is worth noticing that although Acolite-processed R_{rs} have well captured the spatial variations and sharp frontal regions in both datasets, OLI images appeared to be brighter than those of MSI, especially in the red band, which is in accordance with the results shown in Fig. 7 and Table. IV. The MAPE (> 11%) is highest in the R_{rs}(655 nm) products. The lower R_{rs} values are evident in all the MSI products. These differences may be attributed due to a change in atmospheric variables such as aerosols within the short (±30 minutes) time-difference between OLI-MSI images, the differences in the spectral bands of MSI and OLI shown in Table. I, the image artifacts more pronounced in MSI images for this example or inaccurate removal of sea surface reflection due to different sun-sensor geometry between the two senors [65]. Furthermore, some negative retrievals are also observed in the MSI 655 nm band marked with an arrow. The negative R_{rs} values may be due to the over correction of atmospheric effects [7], [66]. Overall, among the three processors, it is demonstrated that Acolite retrieved OLI-MSI R_{rs} products are comparable with similar R_{rs} values range.

2) Comparison OLI-MSI R_{rs} products:* In Fig. 10, we have demonstrated the effectiveness of the proposed BA method using the same OLI-MSI images as in Fig. 9. Note that these image pairs are not used in the training of the BA model. The visual comparison illustrates that the spatial details and variations are preserved in the BA adjusted MSI products (MSI* R_{rs}) with a decrease in the difference between R_{rs} values, for example, the areas indicated by ellipses in Fig. 10. Our results in Fig. 9 and Fig. 10 suggest that Acolite retrieved OLI-MSI* R_{rs} show good agreement and possible future integration of OLI-MSI radiometric data to facilitate consistent, qualitative, and quantitative monitoring of water bodies. The combined use of data products from these sensors will result in an increase in the average revisit time as well as the acquisition of cloud-free images, providing

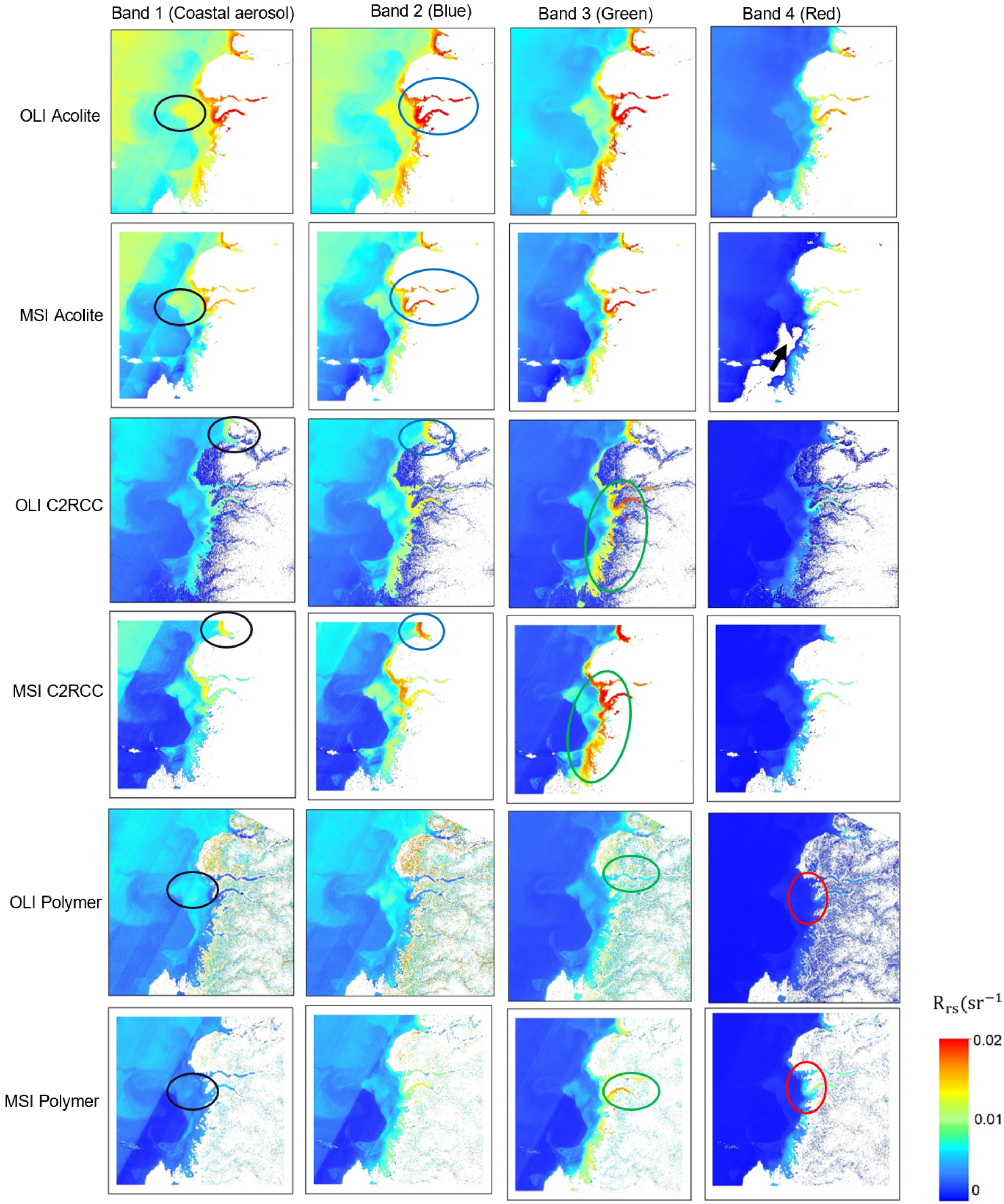

Fig. 9: Comparison between near-simultaneous OLI and MSI R_{rs} products derived via Acolite, C2RCC and Polymer, for the similar bands using the images shown in Fig. 8. The areas indicated by ellipses (colors matching the band number) highlight the similarities/differences in OLI-MSI R_{rs} products when processed via different AC schemes.

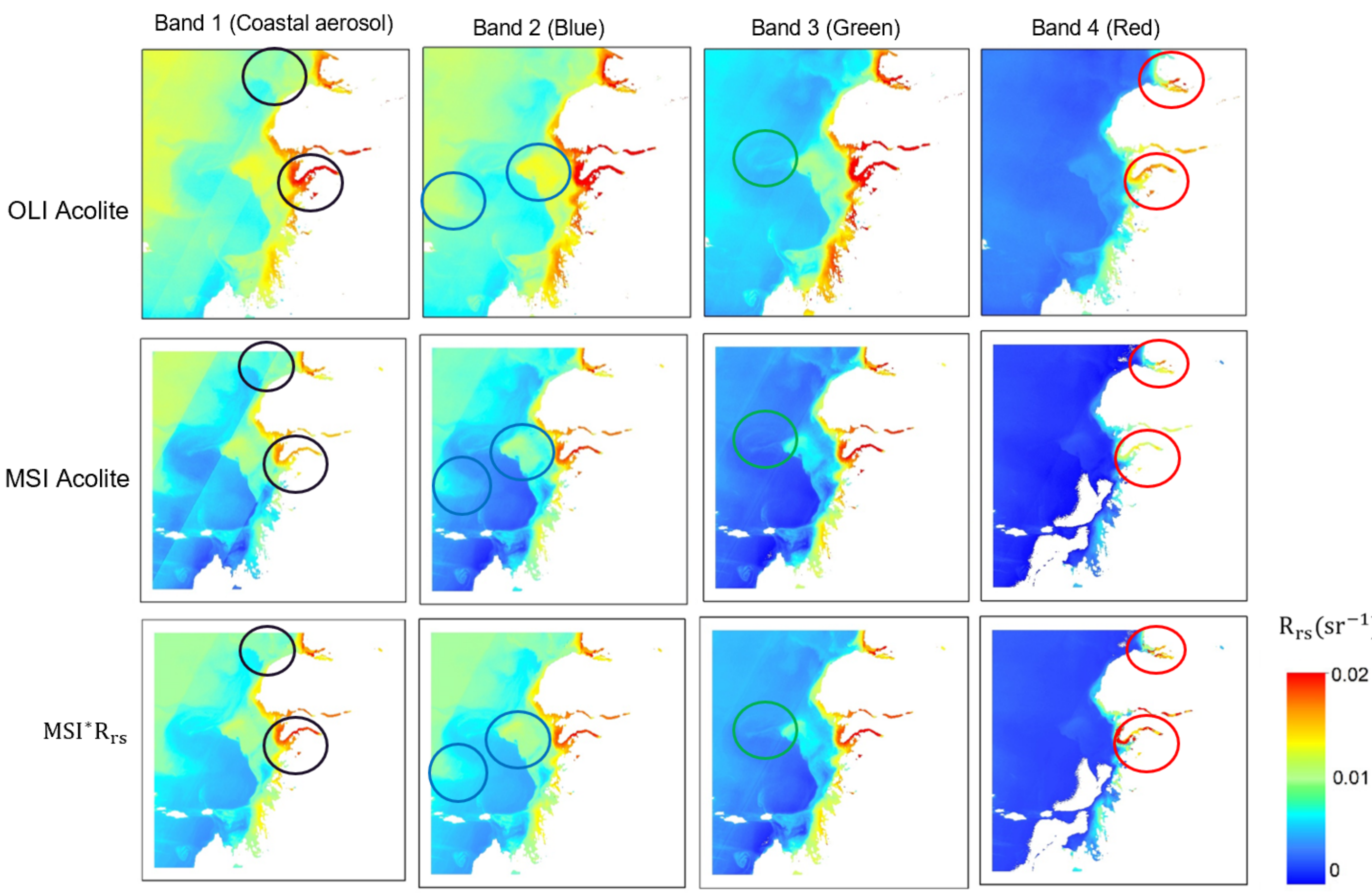

Fig. 10: Comparison between OLI, MSI, and MSI* R_{rs} (after bandpass adjustment) products. The areas indicated by ellipses show that OLI produced higher/lower R_{rs} values compared to MSI. These differences in magnitude are minimized after applying the proposed BA model.

the possibility to increase the frequency of monitoring the dynamics of sensitive aquatic systems at a spatial resolution of 10–60 m. Nonetheless, further research efforts are needed for extensive inter-comparisons of various AC methods under diverse atmospheric and aquatic conditions for coastal and inland water applications.

It should be noted that for spectral alignment of OLI-MSI R_{rs} products, the proposed BA model requires correlation between the MSI and OLI-derived R_{rs} products. In addition, the performance of the BA model depends on the representativeness of the training data. In this work, the proposed model is regionally tuned for the Barents Sea only. However, by incorporating data products from global aquatic systems, the training dataset can be extended. The accuracy of the BA model, like that of other ML algorithms, is determined by the distribution and uncertainties in the $R_r s$ data, which is determined by the performance of AC.

V. Conclusion and Future Work

This paper aimed to improve inter-sensor spectral consistency between S2 MSI and L8 OLI R_{rs} over the Barents Sea. To achieve our objective, we first evaluated the performance of three state-of-the-art AC models, i.e., C2RCC, Acolite (DSF), and Polymer, against in-situ R_{rs} measurements (match-ups). Our analysis demonstrates that all the processors have degraded performance in the coastal aerosol and blue bands. Acolite overestimated R_{rs} values, whereas C2RCC and Polymer have underestimated $R_{rs} > 0.015\,\mathrm{sr}^{-1}$. Comparatively, Acolite is more reliable in the green band with an MAPD of < 10% compared to 24 % and 25% errors using C2RCC and Polymer. In the red band, C2RCC is the top performer, but with a MAPD=14%. Overall, Acolite showed the minimum deviation from the in-situ R_{rs} measurements with an averaged RMSD of $3.3 \times 10^{-3}(\mathrm{sr}^{-1})$, indicating best performance over the Barents Sea.

Regarding inter-comparison of OLI and MSI, our results show that the R_{rs} products processed via Acolite outperform the others and are estimated to range from 8% to 12% with an average RMSD of $7.3 \times 10^{-4}(\mathrm{sr}^{-1})$ in the visible bands. The highest bias was found in the $R_{rs}(665\,\mathrm{nm})$ products with a MAPD and R^2-score of ~12% and 0.71 respectively. The minimum spectral difference is achieved in the $R_{rs}(561\,\mathrm{nm})$ products with R^2-score of ~0.95.

To further minimize the spectral differences in the R_{rs}

products, a neural network-based model was developed to spectrally adjust the S2-A/B radiometry to replicate the spectral bandpasses of L8 for the common bands. The proposed BA model performs pixel-by-pixel transformation of R_{rs} from S2 MSI to L8 OLI equivalent one. After applying the proposed BA model, the spectral difference is significantly reduced from < 10% to 2% (relative to 6-12 % without any spectral adjustment), indicating the effectiveness of the BA for S2 imagery. Our results demonstrate that the proposed BA model is able to accurately reconstruct the spectral properties of OLI from MSI R_{rs} products, which illustrates that MSI observations can be used to complement the R_{rs} products obtained from OLI. For comparison, we have compared the performance of the proposed BA model with the default NASA BA model [9], the OLS regression model. On average, the proposed BA approach reduces the MAPD and RMSD by ~ 2.8% and ~ 30%, compared to ~ 1.1% and ~ 24% improvement caused by the OLS regression model.

The obtained results indicate that L8 OLI and S2 MSI products, ρ_t and R_{rs}, are sufficiently consistent when the vicarious calibration and spectral BA are applied, respectively. Future studies will include exploring the potential application of the proposed spectral BA approach to augment S2 MSI and Sentinel-3 OLCI data products and future hyper-spectral sensors to be comparable to legacy data. An algorithm for better estimating downstream products such as Chl-a and beyond (e.g., phytoplankton absorption spectra), particularly for optically complex waters, should also be developed in further study. To do that, we expect that the BA approach proposed in the present study will aid in better capturing the biogeochemical changes occurring at a smaller spatial scale in the Barents Sea and beyond.

APPENDIX A

This section contains information about OLI-MSI ρ_t inter-comparisons selection and results of spectral difference in their respective products.

A. Inter-comparison of OLI-MSI ρ_t products

For ρ_t inter-comparisons, we have considered near-simultaneous overpasses with a time difference of ±30 minutes with low or no cloud cover and low aerosol loading.

The acquired S2 and L8 images were converted to unit-less (ρ_t) utilizing the calibration coefficients in the metadata and used in the TOA inter-comparisons. As the masking algorithm in S2 Level-1C data does not work well for flagging non-water pixels such as cloud shadow and snow [9], we used an additional masking threshold, i.e., ρ_t (1610 nm) < 0.215 [8]. Similarly, to remove non-water pixels in L8 imagery, in addition to the Quality Assessment (QA) band in L8 Level 1T data, we have used the same masking criteria. If the median over 6 × 6 and 3 × 3 elements window for L8 and S2 MSI was greater than the masking threshold (classified as cloud or land pixels), the inter-comparison window was excluded. Similar to [10], to ensure low aerosol loading, pixels were excluded for inter-comparison if the median value over aerosol optical thickness (AOT) at the 865 nm band, i.e., AOT(865) in a window of 6 × 6 and 3 × 3 pixels for L8 and S2 images, exceeds 0.028 as a cloud screening [8].

B. TOA Reflectance comparison

The scatter plots in Fig. 11 show the spectral difference for the inter-comparisons (OLI-MSI ρ_t pixel pairs) in each band. Overall, MSI-derived ρ_t tends to be greater in magnitude than that of OLI-derived ρ_t in the coastal aerosol, green, and NIR spectral bands. An opposite trend is observed in the blue and green bands (see also Table. V). The highest deviation from the 1:1 line is observed in the ρ_t(865 nm) products.

Values of evaluation metrics enlisted in Table. V permit us to further evaluate the spectral consistency in L8 and S2 ρ_t products. Overall, the spectral difference is minimal in the green band, followed by the red band with RMSLD of 0.012 and 0.013, respectively. Note that to discover the band with the minimum spectral difference between OLI-MSI ρ_t products, we rely on RMSLD more than RMSD since the latter is sensitive to the magnitude of ρ_t. In addition, RMSLD is consistent with the other evaluation metrics in Table. V. The highest R^2(0.97) was observed in the green and red bands, which is in accordance with the results reported in [10] after applying vicarious calibration to simulated TOA reflectance data. It is inferred that the OLI and MSI products agree to within ~4% in the blue bands, < 3% in the green and red bands, without applying any gains. The spectral difference in the NIR band is < 5%, which is comparatively high compared to the visible bands. Referring to Table. V, the high difference in the NIR band is somewhat surprising because the MSI NIR band is quite similar to that of OLI in terms of central wavelength and spectral response profile [63], [67]. In addition, the spectral bandwidth overlap is nearly 80% of the equivalent NIR band of OLI [63]. It may be due to the the lower signal-to-noise ratio of OLI-MSI compared to the visible bands [65]) or limited bandwidth in the NIR band of OLI (2× smaller than the green band) and MSI (~ 1.5× smaller than the green band), as shown in Table. I. The highest RMSLD is observed in the blue and NIR bands, which MRPD further elaborates. It should be noted that MPRD is negative for the blue and positive for the NIR band, which illustrates that the under/overestimation of ρ_t products are band dependent. The MAPD and MRPD in the coastal-aerosol and blue bands are almost similar; however, MRPD is positive in the coastal aerosol band whereas it is negative in the blue band. This highlights positive and negative biases in the MSI ρ_t products in these bands. Among the visible bands, the smallest deviations are observed in the OLI-MSI green band with MAPD and MRPD < 2%. To better understand the uncertainties and their effect on downstream products, we will further evaluate these differences for R_{rs} products in section IV-B.

Restricting the time difference between OLI and MSI overpasses to less than 30 minutes, we assume that the spectral differences illustrated in the spectral plots in Fig. 11

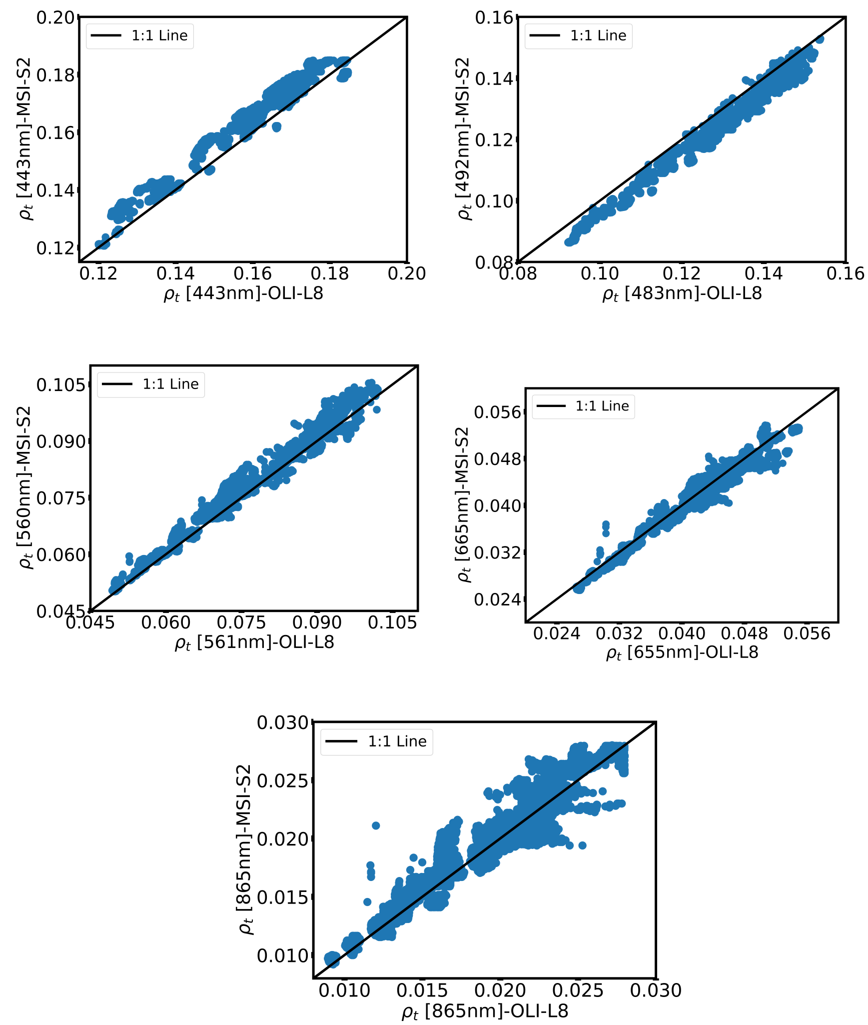

Fig. 11: Inter-comparison of TOA reflectance ρ_t products for L8-S2 pairs. Detailed statistical metrics are available in Table. V.

TABLE V: Intercomparison between Landsat-8 OLI and Sentinel-2 MSI ρ_t product. The number of inter-comparisons (N)=39000 are extracted from near-simultaneous 42 OLI and 71 MSI image pairs.

Bands	RMSD (10^{-3} sr^{-1})	RMSLD	MAPD	MRPD	R^2
443 nm	5.20	0.015	3.05	3.05	0.903
483 nm	5.92	0.023	4.96	-4.96	0.850
561 nm	1.88	0.012	1.57	1.33	0.971
665 nm	1.22	0.013	2.40	-2.15	0.973
865 nm	0.99	0.024	3.65	2.55	0.956

and Table. IV solely originate due to the differences in spectral responses of the individual bands. However, the sensor-induced discrepancies might have been influenced by the difference in the TOA reflectance due to, for example, varying illumination and observation geometries or changing aquatic and atmospheric conditions. To study the differences caused by varying observation geometries of sensors and the bidirectional effects, we computed the view zenith angle per band and performed the inter-comparisons for the pixels with the view zenith angles (VZA) within the $\pm 5°$ range. However, no noticeable improvement was caused in the spectral consistency. As a result, our analysis suggests that ρ_t products of L8 and S2 are consistent in the visible as well as in the NIR channel ($< 4\%$).

Appendix B

This section contains results of spectral difference between Landsat-8 and Sentinel-2-derived R_{rs} products processed via Acolite, C2RCC and Polymer in section IV-B.

Declaration of Competing Interests

None.

TABLE B.1: Comparison of Landsat-8 and Sentinel-2-derived R_{rs} products processed via Acolite, C2RCC and Polymer.

Method	**RMSD** (10^{-3} sr^{-1})	**RMSLD**	R^2	**MAPD**
	Coastal Blue (443 nm)			
Acolite	0.91	0.048	0.846	8.06
C2RCC	1.87	0.144	0.558	24.10
Polymer	1.94	0.186	-0.434	29.96
	Blue (482 nm)			
Acolite	0.94	0.057	0.869	6.68
C2RCC	1.39	0.129	0.762	18.09
Polymer	1.85	0.154	-0.062	26.08
	Green (561 nm)			
Acolite	0.62	0.058	0.946	6.59
C2RCC	1.72	0.149	0.506	18.99
Polymer	0.94	0.109	0.756	19.56
	Red (665 nm)			
Acolite	0.45	0.096	0.714	11.92
C2RCC	1.49	0.329	-0.041	33.17
Polymer	0.45	0.198	0.042	46.07

ACKNOWLEDGMENT

The research is funded by the following projects: The Nansen Legacy (RCN number 276730), CIRFA (RCN number 237906), and partners. The authors would like to acknowledge U.S Geological Survey (USGS) and Copernicus Open Access Hub European space agency (ESA) for providing Landsat-8 (OLI) and Sentinel-2 image archives. The authors would also like to thank Cornelius Quigley and Sidrah Hafeez for proofreading the manuscript. Part of this research was supported by a NASA ROSES project (sponsor award #210319602) and the Japan Aerospace Exploration Agency (JAXA) Global Change Observation Mission-Climate (GCOM-C; the sponsor award #22RT000298) to AM.

REFERENCES

[1] V. Le Fouest, C. Postlethwaite, M. A. M. Maqueda, S. Belanger, and M. Babin, "On the role of tides and strong wind events in promoting summer primary production in the barents sea," *Continental Shelf Research*, vol. 31, no. 17, pp. 1869–1879, 2011.

[2] P. Wassmann, M. Reigstad, T. Haug, B. Rudels, M. L. Carroll, H. Hop, G. W. Gabrielsen, S. Falk-Petersen, S. G. Denisenko, E. Arashkevich *et al.*, "Food webs and carbon flux in the barents sea," *Progress in Oceanography*, vol. 71, no. 2-4, pp. 232–287, 2006.

[3] T. Haug, B. Bogstad, M. Chierici, H. Gjøsæter, E. H. Hallfredsson, Å. S. Høines, A. H. Hoel, R. B. Ingvaldsen, L. L. Jørgensen, T. Knutsen *et al.*, "Future harvest of living resources in the arctic ocean north of the nordic and barents seas: a review of possibilities and constraints," *Fisheries Research*, vol. 188, pp. 38–57, 2017.

[4] P. Dalpadado, K. R. Arrigo, G. L. van Dijken, H. R. Skjoldal, E. Bagøien, A. Dolgov, I. Prokopchuk, and E. Sperfeld, "Climate effects on temporal and spatial dynamics of phytoplankton and zooplankton in the barents sea," *Progress in Oceanography*, p. 102320, 2020.

[5] C. Kuhn, A. de Matos Valerio, N. Ward, L. Loken, H. O. Sawakuchi, M. Kampel, J. Richey, P. Stadler, J. Crawford, R. Striegl *et al.*, "Performance of landsat-8 and sentinel-2 surface reflectance products for river remote sensing retrievals of chlorophyll-a and turbidity," *Remote Sensing of Environment*, vol. 224, pp. 104–118, 2019.

[6] J. Wang, Z. Lee, D. Wang, S. Shang, J. Wei, and A. Gilerson, "Atmospheric correction over coastal waters with aerosol properties constrained by multi-pixel observations," *Remote Sensing of Environment*, vol. 265, p. 112633, 2021.

[7] M. A. Warren, S. G. Simis, V. Martinez-Vicente, K. Poser, M. Bresciani, K. Alikas, E. Spyrakos, C. Giardino, and A. Ansper, "Assessment of atmospheric correction algorithms for the sentinel-2a multispectral imager over coastal and inland waters," *Remote sensing of environment*, vol. 225, pp. 267–289, 2019.

[8] N. Pahlevan, A. Mangin, S. V. Balasubramanian, B. Smith, K. Alikas, K. Arai, C. Barbosa, S. Bélanger, C. Binding, M. Bresciani *et al.*, "Acix-aqua: A global assessment of atmospheric correction methods for landsat-8 and sentinel-2 over lakes, rivers, and coastal waters," *Remote Sensing of Environment*, vol. 258, p. 112366, 2021.

[9] M. Claverie, J. Ju, J. G. Masek, J. L. Dungan, E. F. Vermote, J.-C. Roger, S. V. Skakun, and C. Justice, "The harmonized landsat and sentinel-2 surface reflectance data set," *Remote sensing of environment*, vol. 219, pp. 145–161, 2018.

[10] N. Pahlevan, S. K. Chittimalli, S. V. Balasubramanian, and V. Vellucci, "Sentinel-2/landsat-8 product consistency and implications for monitoring aquatic systems," *Remote sensing of Environment*, vol. 220, pp. 19–29, 2019.

[11] R. Shang and Z. Zhu, "Harmonizing landsat 8 and sentinel-2: A time-series-based reflectance adjustment approach," *Remote Sensing of Environment*, vol. 235, p. 111439, 2019.

[12] Q. Vanhellemont and K. Ruddick, "Acolite for sentinel-2: Aquatic applications of msi imagery," in *Proceedings of the 2016 ESA Living Planet Symposium, Prague, Czech Republic*, 2016, pp. 9–13.

[13] J. Li and D. P. Roy, "A global analysis of sentinel-2a, sentinel-2b and landsat-8 data revisit intervals and implications for terrestrial monitoring," *Remote Sensing*, vol. 9, no. 9, p. 902, 2017.

[14] S. Bélanger, J. K. Ehn, and M. Babin, "Impact of sea ice on the retrieval of water-leaving reflectance, chlorophyll a concentration and inherent optical properties from satellite ocean color data," *Remote Sensing of Environment*, vol. 111, no. 1, pp. 51–68, 2007.

[15] H. K. Zhang, D. P. Roy, L. Yan, Z. Li, H. Huang, E. Vermote, S. Skakun, and J.-C. Roger, "Characterization of sentinel-2a and landsat-8 top of atmosphere, surface, and nadir brdf adjusted reflectance and ndvi differences," *Remote sensing of environment*, vol. 215, pp. 482–494, 2018.

[16] D. Scheffler, D. Frantz, and K. Segl, "Spectral harmonization and red edge prediction of landsat-8 to sentinel-2 using land cover optimized multivariate regressors," *Remote Sensing of Environment*, vol. 241, p. 111723, 2020.

[17] D. P. Roy, H. Zhang, J. Ju, J. L. Gomez-Dans, P. E. Lewis, C. Schaaf, Q. Sun, J. Li, H. Huang, and V. Kovalskyy, "A general method to normalize landsat reflectance data to nadir brdf adjusted reflectance," *Remote Sensing of Environment*, vol. 176, pp. 255–271, 2016.

[18] K. T. Peterson, V. Sagan, and J. J. Sloan, "Deep learning-based water quality estimation and anomaly detection using landsat-8/sentinel-2 virtual constellation and cloud computing," *GIScience & Remote Sensing*, vol. 57, no. 4, pp. 510–525, 2020.

[19] J. Chen and W. Zhu, "Comparing landsat-8 and sentinel-2 top of atmosphere and surface reflectance in high latitude regions: case study in alaska," *Geocarto International*, pp. 1–20, 2021.

[20] N. Pahlevan, S. Sarkar, B. Franz, S. Balasubramanian, and J. He, "Sentinel-2 multispectral instrument (msi) data processing for aquatic science applications: Demonstrations and validations," *Remote sensing of environment*, vol. 201, pp. 47–56, 2017.

[21] P.-A. Herrault, L. Gandois, S. Gascoin, N. Tananaev, T. Le Dantec, and R. Teisserenc, "Using high spatio-temporal optical remote sensing to monitor dissolved organic carbon in the arctic river yenisei," *Remote Sensing*, vol. 8, no. 10, p. 803, 2016.

[22] N. Pahlevan, B. Smith, K. Alikas, J. Anstee, C. Barbosa, C. Binding, M. Bresciani, B. Cremella, C. Giardino, D. Gurlin *et al.*, "Simultaneous retrieval of selected optical water quality indicators from landsat-8, sentinel-2, and sentinel-3," *Remote Sensing of Environment*, vol. 270, p. 112860, 2022.

[23] H. Wang, J. Wang, Y. Cui, and S. Yan, "Consistency of suspended particulate matter concentration in turbid water retrieved from sentinel-2 msi and landsat-8 oli sensors," *Sensors*, vol. 21, no. 5, p. 1662, 2021.

[24] B. P. Page, L. G. Olmanson, and D. R. Mishra, "A harmonized image processing workflow using sentinel-2/msi and landsat-8/oli for mapping water clarity in optically variable lake systems," *Remote Sensing of Environment*, vol. 231, p. 111284, 2019.

[25] E. Mandanici and G. Bitelli, "Preliminary comparison of sentinel-2 and landsat 8 imagery for a combined use," *Remote Sensing*, vol. 8, no. 12, p. 1014, 2016.

[26] P. Li, Y. Ke, J. Bai, S. Zhang, M. Chen, and D. Zhou, "Spatiotemporal dynamics of suspended particulate matter in the yellow river estuary, china during the past two decades based on time-series landsat and sentinel-2 data," *Marine Pollution Bulletin*, vol. 149, p. 110518, 2019.

[27] M. A. Warren, S. G. Simis, and N. Selmes, "Complementary water quality observations from high and medium resolution sentinel sensors by aligning chlorophyll-a and turbidity algorithms," *Remote Sensing of Environment*, vol. 265, p. 112651, 2021.

[28] S. Hafeez, M. S. Wong, S. Abbas, and M. Asim, "Evaluating landsat-8 and sentinel-2 data consistency for high spatiotemporal inland and coastal water quality monitoring," *Remote Sensing*, vol. 14, no. 13, p. 3155, 2022.

[29] S. Xie, L. Sun, L. Liu, and X. Liu, "Global cross-sensor transformation functions for landsat-8 and sentinel-2 top of atmosphere and surface reflectance products within google earth engine," *IEEE Transactions on Geoscience and Remote Sensing*, 2022.

[30] S. W. Bailey and P. J. Werdell, "A multi-sensor approach for the on-orbit validation of ocean color satellite data products," *Remote Sensing of Environment*, vol. 102, no. 1-2, pp. 12–23, 2006.

[31] C. Brockmann, R. Doerffer, M. Peters, S. Kerstin, S. Embacher, and A. Ruescas, "Evolution of the c2rcc neural network for sentinel 2 and 3 for the retrieval of ocean colour products in normal and extreme optically complex waters," in *Living Planet Symposium*, vol. 740, 2016, p. 54.

[32] Q. Vanhellemont, "Adaptation of the dark spectrum fitting atmospheric correction for aquatic applications of the landsat and sentinel-2 archives," *Remote Sensing of Environment*, vol. 225, pp. 175–192, 2019.

[33] F. Steinmetz, P.-Y. Deschamps, and D. Ramon, "Atmospheric correction in presence of sun glint: application to meris," *Optics express*, vol. 19, no. 10, pp. 9783–9800, 2011.

[34] M. Asim, C. Brekke, A. Mahmood, T. Eltoft, and M. Reigstad, "Improving chlorophyll-a estimation from sentinel-2 (msi) in the barents sea using machine learning," *IEEE Journal of Selected Topics in Applied Earth Observations and Remote Sensing*, 2021.

[35] Q. Vanhellemont and K. Ruddick, "Atmospheric correction of metre-scale optical satellite data for inland and coastal water applications," *Remote sensing of environment*, vol. 216, pp. 586–597, 2018.

[36] K. P. Klein, H. Lantuit, B. Heim, D. Doxaran, B. Juhls, I. Nitze, D. Walch, A. Poste, and J. E. Søreide, "The arctic nearshore turbidity algorithm (anta)-a multi sensor turbidity algorithm for arctic nearshore environments," *Science of Remote Sensing*, vol. 4, p. 100036, 2021.

[37] C. D. Mobley, *Light and water: radiative transfer in natural waters.* Academic press, 1994.

[38] K. G. Ruddick, V. De Cauwer, Y.-J. Park, and G. Moore, "Seaborne measurements of near infrared water-leaving reflectance: The similarity spectrum for turbid waters," *Limnology and Oceanography*, vol. 51, no. 2, pp. 1167–1179, 2006.

[39] J. Wei, Z. Lee, R. Garcia, L. Zoffoli, R. A. Armstrong, Z. Shang, P. Sheldon, and R. F. Chen, "An assessment of landsat-8 atmospheric correction schemes and remote sensing reflectance products in coral reefs and coastal turbid waters," *Remote sensing of environment*, vol. 215, pp. 18–32, 2018.

[40] Q. Vanhellemont, "Sensitivity analysis of the dark spectrum fitting atmospheric correction for metre-and decametre-scale satellite imagery using autonomous hyperspectral radiometry," *Optics Express*, vol. 28, no. 20, pp. 29 948–29 965, 2020.

[41] "ESA Sentinel-2 MSI Radiometric Performance," accessed 2022-01-04. [Online]. Available: https://dragon3.esa.int/web/sentinel/technical-guides/sentinel-2-msi/performance

[42] P. K. Roy, M. B. Roy, and S. Pal, *Advances in Water Resources Management for Sustainable Use.* Springer Nature, 2021, vol. 131.

[43] "Landsat-8 science," accessed 2022-01-04. [Online]. Available: https://landsat.gsfc.nasa.gov/satellites/landsat-8/

[44] C. D. Mobley, L. K. Sundman, C. O. Davis, J. H. Bowles, T. V. Downes, R. A. Leathers, M. J. Montes, W. P. Bissett, D. D. Kohler, R. P. Reid *et al.*, "Interpretation of hyperspectral remote-sensing imagery by spectrum matching and look-up tables," *Applied Optics*, vol. 44, no. 17, pp. 3576–3592, 2005.

[45] J. R. Schott, A. Gerace, C. E. Woodcock, S. Wang, Z. Zhu, R. H. Wynne, and C. E. Blinn, "The impact of improved signal-to-noise ratios on algorithm performance: Case studies for landsat class instruments," *Remote Sensing of Environment*, vol. 185, pp. 37–45, 2016.

[46] B. Markham, J. Barsi, G. Kvaran, L. Ong, E. Kaita, S. Biggar, J. Czapla-Myers, N. Mishra, and D. Helder, "Landsat-8 operational land imager radiometric calibration and stability," *Remote Sensing*, vol. 6, no. 12, pp. 12 275–12 308, 2014.

[47] P. Qin, S. G. Simis, and G. H. Tilstone, "Radiometric validation of atmospheric correction for meris in the baltic sea based on continuous observations from ships and aeronet-oc," *Remote sensing of environment*, vol. 200, pp. 263–280, 2017.

[48] E. López-Iñesta, F. Grimaldo, and M. Arevalillo-Herráez, "Combining feature extraction and expansion to improve classification based similarity learning," *Pattern Recognition Letters*, vol. 93, pp. 95–103, 2017.

[49] M. Asim, C. Brekke, A. Mahmood, T. Eltoft, and M. Reigstad, "Ocean color net (ocn) for the barents sea," in *IGARSS 2020-2020 IEEE International Geoscience and Remote Sensing Symposium.* IEEE, 2020, pp. 5881–5884.

[50] N. Almaadeed, M. Asim, S. Al-Maadeed, A. Bouridane, and A. Beghdadi, "Automatic detection and classification of audio events for road surveillance applications," *Sensors*, vol. 18, no. 6, p. 1858, 2018.

[51] I. Goodfellow, Y. Bengio, and A. Courville, *Deep Learning.* MIT Press, 2016, http://www.deeplearningbook.org.

[52] S. Ioffe and C. Szegedy, "Batch normalization: Accelerating deep network training by reducing internal covariate shift," *arXiv preprint arXiv:1502.03167*, 2015.

[53] X. Glorot and Y. Bengio, "Understanding the difficulty of training deep feedforward neural networks," in *Proceedings of the thirteenth international conference on artificial intelligence and statistics*, 2010, pp. 249–256.

[54] M. Abadi, A. Agarwal, P. Barham, E. Brevdo, Z. Chen, C. Citro, G. S. Corrado, A. Davis, J. Dean, M. Devin, S. Ghemawat, I. Goodfellow, A. Harp, G. Irving, M. Isard, Y. Jia, R. Jozefowicz, L. Kaiser, M. Kudlur, J. Levenberg, D. Mané, R. Monga, S. Moore, D. Murray, C. Olah, M. Schuster, J. Shlens, B. Steiner, I. Sutskever, K. Talwar, P. Tucker, V. Vanhoucke, V. Vasudevan, F. Viégas, O. Vinyals, P. Warden, M. Wattenberg, M. Wicke, Y. Yu, and X. Zheng, "TensorFlow: Large-scale machine learning on heterogeneous systems," 2015, software available from tensorflow.org. [Online]. Available: https://www.tensorflow.org/

[55] Y. Xu, L. Feng, D. Zhao, and J. Lu, "Assessment of landsat atmospheric correction methods for water color applications using global aeronet-oc data," *International Journal of Applied Earth Observation and Geoinformation*, vol. 93, p. 102192, 2020.

[56] T. J. Breider, L. J. Mickley, D. J. Jacob, Q. Wang, J. A. Fisher, R. Y.-W. Chang, and B. Alexander, "Annual distributions and sources of arctic aerosol components, aerosol optical depth, and aerosol absorption," *Journal of Geophysical Research: Atmospheres*, vol. 119, no. 7, pp. 4107–4124, 2014.

[57] M. Á. Obregón, G. Rodrigues, M. J. Costa, M. Potes, and A. M. Silva, "Validation of esa sentinel-2 l2a aerosol optical thickness and columnar water vapour during 2017–2018," *Remote Sensing*, vol. 11, no. 14, p. 1649, 2019.

[58] P. R. Renosh, D. Doxaran, L. D. Keukelaere, and J. I. Gossn, "Evaluation of atmospheric correction algorithms for sentinel-2-msi and sentinel-3-olci in highly turbid estuarine waters," *Remote Sensing*, vol. 12, no. 8, p. 1285, 2020.

[59] H. Liu, X. He, Q. Li, X. Hu, J. Ishizaka, S. Kratzer, C. Yang, T. Shi, S. Hu, Q. Zhou *et al.*, "Evaluation of ocean colour atmospheric correction methods for sentinel-3 olci using global automatic in-situ observations," *IEEE Transactions on Geoscience and Remote Sensing*, 2021.

[60] S. Kratzer and M. Plowey, "Integrating mooring and ship-based data for improved validation of olci chlorophyll-a products in the baltic sea," *International Journal of Applied Earth Observation and Geoinformation*, vol. 94, p. 102212, 2021.

[61] C. R. McClain, G. Meister *et al.*, "Mission requirements for future ocean-colour sensors." 2012.

[62] F. Mélin, G. Sclep, T. Jackson, and S. Sathyendranath, "Uncertainty estimates of remote sensing reflectance derived from comparison of ocean color satellite data sets," *Remote Sensing of Environment*, vol. 177, pp. 107–124, 2016.

[63] R. Chastain, I. Housman, J. Goldstein, M. Finco, and K. Tenneson, "Empirical cross sensor comparison of sentinel-2a and 2b msi, landsat-8 oli, and landsat-7 etm+ top of atmosphere spectral characteristics over the conterminous united states," *Remote sensing of environment*, vol. 221, pp. 274–285, 2019.

[64] C. Del Castillo, S. Platnick, and D. Antoine, "Pre-aerosol, clouds, and ocean ecosystem (pace) mission science definition team report," in *Proceedings of the Ocean Carbon and Biogeochemistry Workshop, Woods Hole, MA, USA*, 2012, pp. 16–19.

[65] N. Pahlevan, B. Smith, C. Binding, and D. O'Donnell, "Spectral band adjustments for remote sensing reflectance spectra in coastal/inland waters," *Optics Express*, vol. 25, no. 23, pp. 28 650–28 667, 2017.

[66] Q. Vanhellemont and K. Ruddick, "Advantages of high quality swir bands for ocean colour processing: Examples from landsat-8," *Remote Sensing of Environment*, vol. 161, pp. 89–106, 2015.

[67] S. Li, S. Ganguly, J. L. Dungan, W. Wang, R. R. Nemani *et al.*, "Sentinel-2 msi radiometric characterization and cross-calibration with landsat-8 oli," *Advances in Remote Sensing*, vol. 6, no. 02, p. 147, 2017.